Materials Science & Engineering A 935 (2025) 148383

Contents lists available at ScienceDirect

Materials Science & Engineering A

journal homepage: www.elsevier.com/locate/msea

Global 3D-gradient-structured steel sheets with superior strength-ductility combination

Yindong Shi [a,b], Aojie Zhang [a], Lina Wang [a], Tao Liu [a], Xiliang Zhang [a,*], Xinrui Yang [a], Zhenguo Xing [a], Yuntian Zhu [b,**]

[a] Hebei Key Laboratory of Wear-resistant Metallic Materials with High Strength and Toughness/Whole Processes of High Quality Fastener Application Technology Research Center of Universities in Hebei Province, Hebei University of Engineering, Handan, 056038, China
[b] Department of Materials Science and Engineering, City University of Hong Kong, Hong Kong, 999077, China

ARTICLE INFO

Keywords:
Global 3D-gradient-structure
Strength-ductility combination
Unique TRIP effect
HDI work hardening
Stainless steel sheet

ABSTRACT

Global gradient structures (GGS) from core to surface processed by twisting have been reported to possess exceptional strength-ductility combinations. However, it is hard to apply this technique to sheet (plate) samples because of their lower axial symmetry. Here, we report a novel 3D-GGS produced in a 304 stainless steel (304ss) sheet using cyclic twisting. The 3D-GGS 304ss sheets exhibited much better strength-ductility combinations than GGS 304ss rods due to their more pronounced heterostructural effects. During the tensile testing, a unique transformation-induced plasticity (TRIP) effect was activated in which reverse martensitic transformation ($\alpha' \rightarrow \gamma$) was first activated, then transited to forward martensitic transformation ($\gamma \rightarrow \alpha'$) after some strain. Both the reverse and forward TRIP effects contributed to higher ductility. In addition, the 3D-structures also produced hetero-deformation induced (HDI) work hardening to retain ductility. This work developed a practical approach to constructing 3D-GGS to enhance integrated performances of metal sheets and components without changing their geometries.

1. Introduction

The automotive, marine and other industries urgently require advanced materials with superior integrated properties or functionalities. Unfortunately, the properties of metallic materials are often mutually exclusive; for instance, there is typically a trade-off between strength and ductility [1], as well as between magnetization and coercivity [2,3]. To address these challenges, materials scientists have been developing heterostructured materials that are composed of distinct zones designed to enhance integrated properties [4–6]. To date, a variety of heterostructures have been fabricated in metals and alloys, including heterogeneous lamella structures [7,8], layered structures [9–11], gradient structures [12–15], dual- and multi-heterostructures [16–23] and composite structures [24–28]. The superior integrated properties of heterostructured materials arise from the interactive coupling between the hetero-zones, which can produce a synergistic effect [1–4]. Notably, HDI strengthening and HDI strain hardening are achieved through the pile-up of geometrically necessary dislocations (GNDs) near zone boundaries to accommodate the mechanical incompatibility and strain gradient between different zones, thereby simultaneously enhancing strength and ductility [3,7,29,30].

As one of the most popular heterostructures, the gradient structure has been produced near the surface of various metallic materials, including Cu [12,31], IF steel [30,32], Al [33] and stainless steel [34,35] through surface severe plastic deformation. However, in larger samples, the volume fraction of the gradient nanograined layer tends to be comparatively low, which may limit the overall enhancement of their mechanical properties. Increasing the volume fraction of the gradient nanostructure could significantly improve integrated performances of large samples [31,36]. An alternative approach involves creating a global gradient structures (GGS) from core to surface by employing twisting processes on metal rods, which can achieve exceptional combinations of strength and ductility [13,37–40]. For example, the yield strength of stainless steel and high-entropy alloy can be enhanced by 1∼2 times through the GGS without significant loss of ductility [13,38]. In addition to rod-shaped samples or components, engineering

* Corresponding author.
** Corresponding author.
E-mail addresses: xlzhang@hebeu.edu.cn (X. Zhang), y.zhu@cityu.edu.hk (Y. Zhu).

https://doi.org/10.1016/j.msea.2025.148383
Received 16 February 2025; Received in revised form 4 April 2025; Accepted 21 April 2025
Available online 23 April 2025

applications often involve various structures in the form of sheets or plates. However, applying the twisting technique to sheet (plate) samples poses challenges due to their lower axial symmetry when constructing GGS to enhance integrated performances. It is expected that novel GGS structures are produced in sheet samples through twisting processing due to the mutual constraints between different sample zones. Additionally, potential engineering applications of twisting technique needs further exploration.

Here, we present a novel three dimensional global gradient structure (3D-GGS) created in 304ss sheets using a cyclic twisting (CT) technique, which features a gradual variation in both the dislocation density and the α'-martensite content across multiple dimensions and routes. The innovative 3D-GGS allows 304ss sheets to achieve significantly better strength-ductility combinations than GGS 304ss rods, which is attributed to the more pronounced heterostructural effects. Corresponding mechanisms for strengthening and toughening will be studied and discussed. The current study highlights a promising approach to developing novel 3D-GGS structures and enhancing the strength-ductility combinations of metal sheets (plates) and components at a low cost, without altering their geometries.

2. Materials and experimental procedures

The raw materials for this study were commercial 304ss sheets with a chemical composition of Fe-0.04C-0.38Si-1.16Mn-18.24Cr-8.02Ni-0.029P-0.005N (wt.%). The 304ss sheets, approximately 2 mm thick, were austenitized at 900 °C for 1 h to achieve a coarse-grained (CG) microstructure. Dog-bone-shaped specimens with a gauge dimension of 40 × 5 × 2 mm^3 were machined from CG sheets using electrical discharge machining. Subsequently, the dog-bone-shaped specimens were subjected to cyclic twisting (CT) processing at room temperature. The CT parameters were as follows: CT angle amplitudes ranging from 10° to 50°, with a CT rate of 1°/s and a CT cycle of 60. Based on the angle amplitudes used during the CT processing, the samples were designated as CT-10, CT-20, CT-30, CT-40, and CT-50. Diagrams of dog-bone-shaped samples before and after CT process, and after tensile deformation were shown in Fig. S1.

Vickers microhardness (*Hv*) measurements were conducted at the cross-section and the top surface of the CG and CT-treated 304ss sheets before and after tensile deformation. The *Hv* tests were performed under a load of 9.8 N with a duration of 10 s. Each *Hv* average was obtained from three repeated measurements taken at different cross-sections. Room temperature mechanical properties of the CG and CT-treated samples were investigated by tensile tests at a nominal strain rate of 5.0 × 10^{-4} s^{-1}. Loading-unloading-reloading (LUR) tests were conducted at a loading speed of 5.0 × 10^{-4} s^{-1} and an unloading speed of 400 N/min. During the tensile and LUR tests, a contact extensometer with a gauge length of 25 mm was used to accurately measure the strain. Three specimens, with a gauge dimension of 40 × 5 × 2 mm^3, of each condition were repeatedly investigated to ensure reliable mechanical properties.

In situ synchrotron-based high energy (HE) X-ray studies of the cyclic twisting (CT) treated samples during tension were conducted at DESY P21.1 High Energy X-Ray Diffraction for Physics and Chemistry at the Swedish Beamline. The beamline operates at fixed photon energies, primarily at 100 keV. The beam size is about 1 × 1 mm^2, and the wavelength of HE X-ray is 0.12225 nm. For HE X-ray studies, 304ss samples with a gauge dimension of 10 × 3 × 2 mm^3 were subjected to the CT process at an angle amplitude of 30°, CT rate of 1°/s and CT cycles of 15, approximately gaining identical shear strain to that of the CT-30 sample. In-situ uniaxial tensile tests were carried out at a nominal strain rate of 5 × 10^{-4} s^{-1} to ensure good data statistics. Single peak fitting was used to calculate orientation-specific lattice spacing, lattice strain, average phase stress and volume fraction of constituent phases. (111), (200), (220), (311), (222) peaks for γ austenite, (10-10), (0002) peaks for ε martensite and (110), (200), (211), (220) peaks for α' martensite were fitted, respectively. Electron backscatter diffraction (EBSD) and transmission electron microscopy (TEM) observations were carried out to characterize the microstructures of the CT-processed 304ss before and after tensile deformation. The samples for TEM observations were mechanically thinned by sandpapers and then ion thinned. The samples for EBSD observations were mechanically ground and electrochemically polished. The EBSD data were further analyzed using the OIM Analysis and Aztec Crystal softwares to obtain IQ, grain boundary and phase images and the distributions of grain size, Kernel Average Misorientation (KAM) and GNDs. For calculating the GNDs density, a bin size of 5 × 5, a step size of 170 nm and a threshold angle of 5° were adopted. The HRTEM images were treated by the Digital Micrograph software to acquire the fast Fourier transform (FFT) patterns and inverse FFT images.

3. Results and discussion

3.1. Mechanical properties

The typical tensile stress-strain curves (#1–5) of the CG and cyclic twisting (CT) treated 304ss are illustrated in Fig. 1a, allowing for the determination of their mechanical properties, as shown in Fig. 1b and Table S1. The CG sample (#1) exhibits a low yield strength of ~270.4 MPa and a high uniform elongation of ~56.2 %. Notably, the yield strength of the CT-processed samples (#2–5) gradually increases from ~352.9 MPa to ~535.6 MPa. This increase is accompanied by a slight reduction in uniform elongation, which decreases from ~56.4 % to ~44.1 %. This trend follows an inverse banana-shaped pattern (Fig. 1b), with increasing the CT angle amplitude from 10° to 50°. Consequently, an excellent combination of high strength and ductility is achieved, as evidenced by the increased strain energy density (the stress-strain curve area) and improved yield strength (Fig. 1c).

The work hardening rates (WHR) of the CG and CT-treated 304ss were analyzed to investigate the physical origin of the exceptional strength-ductility combinations, as illustrated in Fig. 1d. The WHR of the CG sample exhibits a three-stage evolution. Initially, it decreases to approximately 1800 MPa at a true strain of ~10 %, and then it increases to ~3090 MPa at a true strain of ~24 %. Finally, the WHR drops again until a fracture occurs. The initial decrease in work hardening rate is primarily influenced by the planar slip of partials and the formation of ε-martensite [34,41]. The subsequent up-turning of the WHR is due to the strain-induced martensitic transformation, known as the TRIP effect [34,35,42]. After CT processing, the 304ss also exhibits multistage work hardening behavior, similar to that of the CG one. However, the starting strain values of WHR up-turning move to lower strain levels with the increase in CT angle amplitude, akin to that of the gradient nanograined 304ss [34]. Interestingly, the amplitude of the WHR increase from trough to peak is nearly the same (~1000 MPa) for the CT-treated samples, comparable to the ~1300 MPa observed in the CG one. After reaching the peak, the WHR decreases more slowly for the CT-treated samples compared to the CG sample. Therefore, the up-turning at the low strain levels and the slower decrease at the high strain ranges of the WHR contribute to the high work hardening capacities and ductility observed in CT-treated samples (Fig. 1(a and b)).

Shown in Fig. 2a is the *Hv* distribution across the cross-section of the CT-30 304ss. Assisted by contour lines, *Hv* gradients can be observed in multiple dimensions and along various routes. Fig. 2(b–e) show how *Hv* varies with depth in the CT-30 304ss along different routes, as shown in Fig. 2f. Specifically, along route i (● in Fig. 2b), the *Hv* initially decreases from one side toward the core and then increases toward the opposite side. In route ii (Fig. 2c), the *Hv* gradient layers of ~800 μm are observed on both sides, with only a slight enhancement and relatively stable *Hv* values in intermediate regions. Conversely, routes iii (the top surface) and iv exhibit an unexpected reverse *Hv* gradient (Fig. 2d,e), where hardness increases from each side toward the core. In comparison, the *Hv* values in the CG sample remain nearly equivalent, averaging

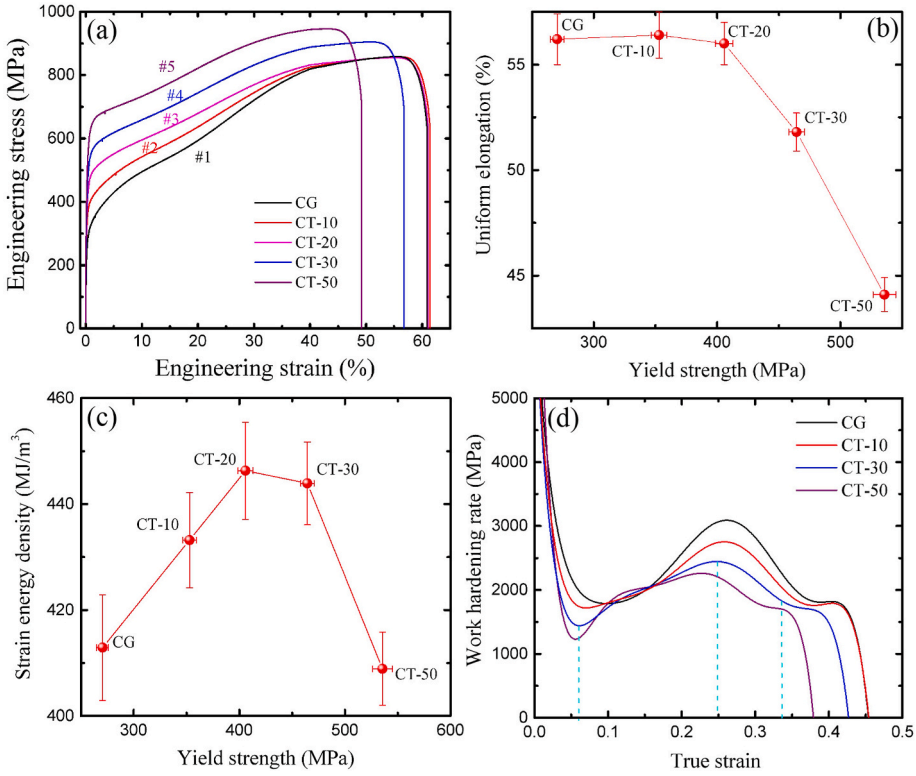

Fig. 1. (a) Tensile engineering stress-strain curves, (b) Yield strength versus uniform elongation, (c) Yield strength versus strain energy density and (d) Dependence of work hardening rates on the applied strain for CG and CT-processed 304ss sheets.

~184.8 (■ in Fig. 2b), indicating a homogeneous structure. As reported by previous studies [30,35], the *Hv* gradient signifies a microstructural gradient. The *Hv* gradients along different dimensions and routes demonstrate the production of a novel GGS with multiple zone boundaries in 304ss sheets due to the CT processing.

Fig. 3(a–d) plot the *Hv* evolution along different routes for the CG and CT-30 samples after undergoing tensile deformation with strains ranging from 5.3 % to 40 %. As the tensile strain increases, the *Hv* value at any location along all routes steadily rises, indicating a continuous work hardening behaviour, similar to that observed in GGS stainless steel and high-entropy alloy [13,38]. However, the *Hv* increments along various routes occur asynchronously during tensile deformation (Fig. 3a-c), suggesting the presence of hetero-deformation. Moreover, with proceeding tensile strain, the *Hv* gradient remains evident in route i (Fig. 3a), however, it becomes weaker and even negligible in routes ii and iii (Fig. 3(b and c)). By contrast, the *Hv* values of the CG sample along route iii remain constant throughout the entire tensile deformation (Fig. 3d). Also, after ~40 % tensile strain, the CT-30 sample manifest higher *Hv* values, indicating a stronger hardening ability compared to the CG sample.

To probe the origin of the exceptional strength and ductility observed in CT-treated 304ss, the HDI stresses and their evolution under applied true strain for both the CT-30 and CG samples were examined using LUR tensile testing, as shown in Fig. 4. The hysteresis loops for the two specimens become more pronounced with increasing applied strain (Fig. 4(a and b)). Notably, the CT-30 sample exhibits higher HDI stresses at the same applied strain compared to the CG sample, which contributes to the enhancement in yield strength and flow stress (Fig. 1). The gradual increase in HDI stress (Fig. 4c), indicative of HDI work hardening, occurs through the entire stage of uniform plastic deformation, which helps in retaining high WHR and uniform elongation in the CT-30 sample.

3.2. Microstructural characterizations

EBSD observations were conducted to analyze the phase and dislocation distributions of the CT-30 sample. The EBSD phase images and grain boundary images (Fig. 5(a and b) and S2) from the cross-section locations (Fig. 5c) show interesting results. At locations I and IV (Fig. 5(a_I,a_{IV})), only small amounts of α' martensite (orange phase) are present, with volume fractions of ~2.0 % and ~1.6 %, respectively. In comparison, significantly higher amounts of α' martensite are exhibited at locations II and III (Fig. 5(a_{II},a_{III})), with volume fractions of ~18.4 % and ~23.9 %. Additionally, the densities of low-angle grain boundary (indicated by red dots), considered dislocation-type boundary, are also higher at locations II and III (Fig. 5, S2(b_{II},b_{III})) than those at locations I and IV (Fig. 5, S2(b_I,b_{IV})). This observation supports the idea that a higher density of dislocations was introduced at former locations [13, 38]. After CT processing, the average grain sizes of γ austenite remain nearly unchanged at all four locations (Fig. S3). The EBSD KAM results (Fig. S4 and S5) indicate much larger KAM misorientations at locations II and III compared to I and IV. These observations suggest that larger KAM misorientations—associated with a higher GND density—are influenced by both the strain gradient and the martensitic transformation of $\gamma \rightarrow \alpha'$. To sum up, both the α'-martensite volume fraction and the dislocation density exhibit a gradient change along specific routes (e.g., i to iv). In addition, microstructural heterogeneity is still present between the γ-austenite and α'-martensite. Therefore, a novel 3D-GGS is constructed in 304ss sheets via CT processing. The dual gradient of dislocation density and α'-martensite volume fraction is responsible for the observed *Hv* gradients (Fig. 2). The induction of α'-martensite and dislocations contributes to the enhancement of yield strength and *Hv* (Figs. 1 and 2).

Fig. 6 displays the superimposed EBSD IQ plus phase images of the CG and CT-30 samples subjected to tensile strains. At ~5.3 % tensile strain, the CG sample exhibits a volume fraction of α' martensite (orange phase) of only ~1.5 % (Fig. 6a_1). Meanwhile, there is a noticeable

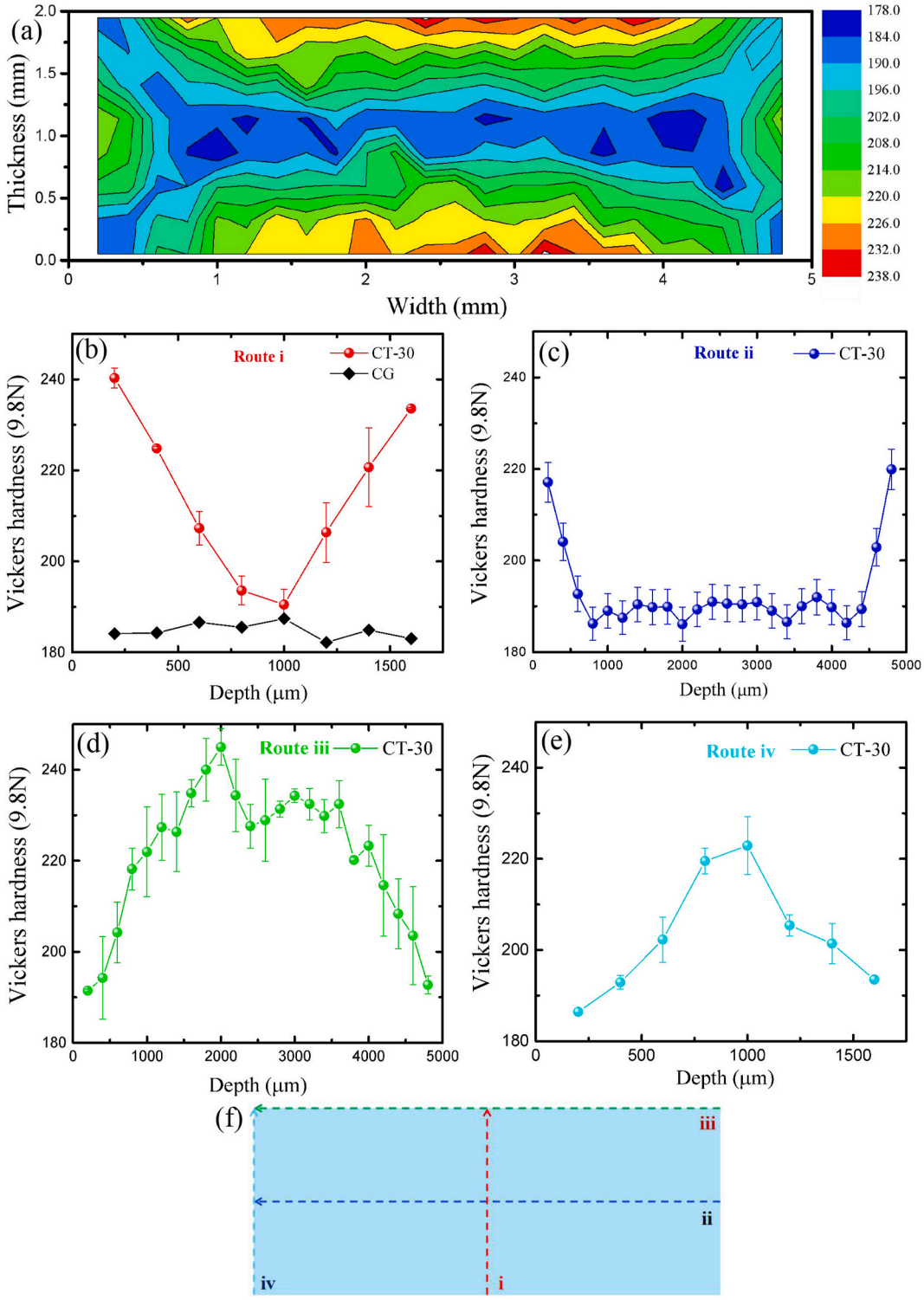

Fig. 2. (a) *Hv* distribution across the cross-section of CT-30 304ss. Evolution of *Hv* with depth along route i (b), route ii (c), route iii (d) and route iv (e) of CG and CT-30 304ss. (f) Schematic of routes of *Hv* measurements.

increase in KAM misorientation and GND density (Fig. 7(a_1,f)). As the tensile strain increases to ~24 % and ~40 % (Fig. 6(a_2,a_3)), the volume fraction of α' martensite rises to ~29.2 % and 60.8 % (see ■ in Fig. 6d), respectively, indicating a continuous martensitic transformation of $\gamma \rightarrow \alpha'$. This ongoing martensitic transformation helps explain the WHR upturn and high ductility displayed by the CG sample (#1 in Fig. 1). In contrast, after a tensile strain of ~5.3 %, the CT-30 sample shows a decrease in volume fraction of α' martensite at locations II and III, dropping to about 5.9 % and 0.4 % (Fig. 6(c_1,d_1)), indicating a reverse martensitic transformation from α' back to γ. A greater number of twinning boundaries are observed post-reverse transformation relative to before (Fig. S6), suggesting that the reverted γ austenite establishes a twinning relation with the original γ matrix, as discussed in previous studies on high-entropy alloys [43–45]. Furthermore, compared to the CG sample under ~5.3 % tensile strain (see Fig. S7), an evident refinement of γ grains supports the occurrence of the reverse transformation,

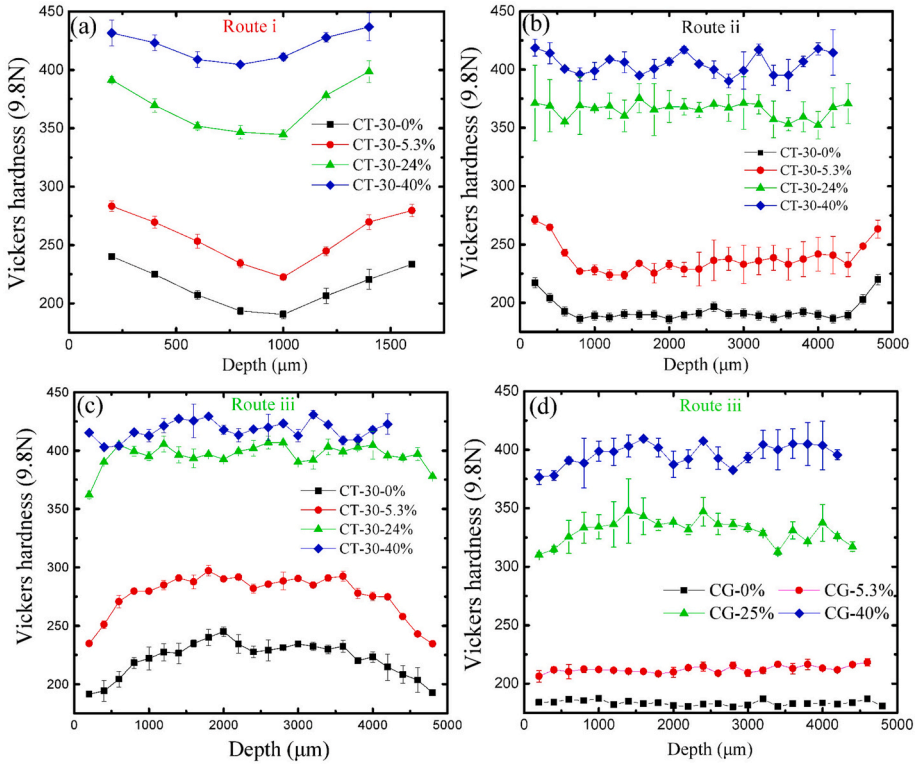

Fig. 3. Evolution of *Hv* with depth along route i (a), route ii (b), route iii (c) of CT-30 304ss, (d) Evolution of *Hv* with depth along route iii of the CG 304ss after tensile deformation with various strains.

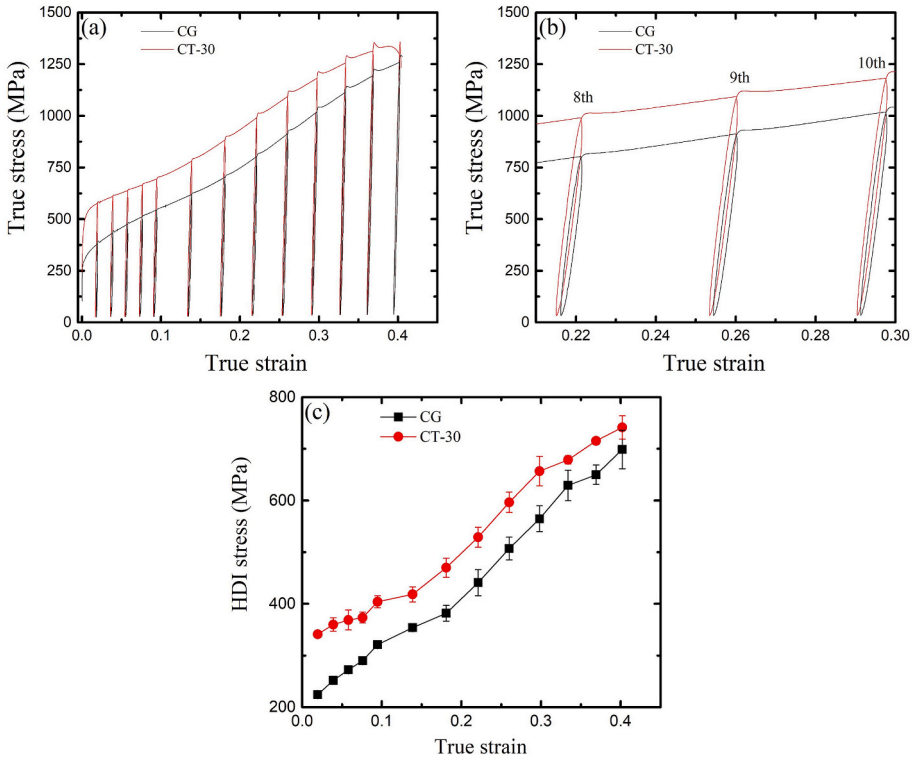

Fig. 4. (a) LUR stress-strain curves of CG and CT-30 304ss, (b) Enlarged image of the 8th, 9th and 10th hysteresis loops of (a), (c) Dependence of HDI stress on true strain.

which has been proven in 304ss [34,41]. XRD investigations were conducted on the surface of the CT-30 sample before and after 5.3 % tensile strain (see Fig. S8). After ~5.3 % tensile strain, the noticeable decrease in α' diffraction peak intensity and the corresponding increase in γ peaks definitively confirms the occurrence of the reverse martensitic transformation.

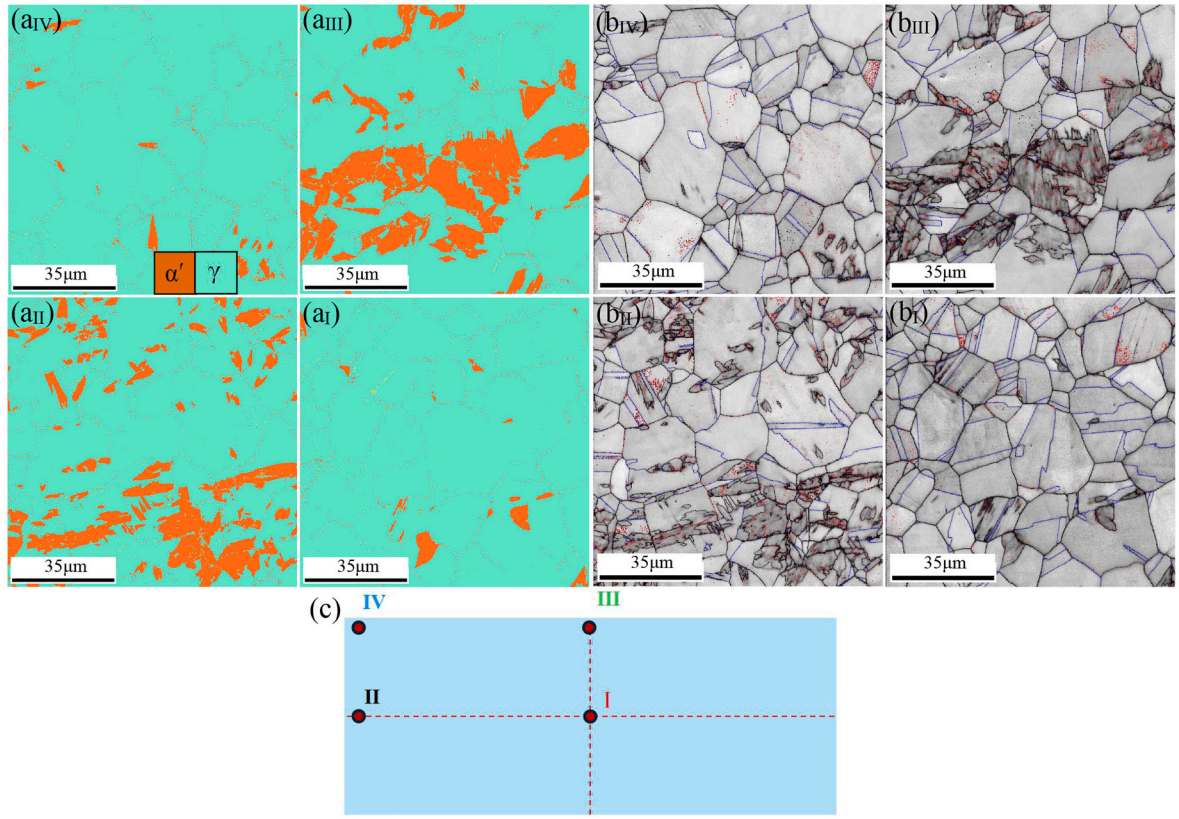

Fig. 5. (a) EBSD phase images and (b) EBSD grain boundary images of CT-30 304ss taken at locations I (a_I, b_I), II (a_{II}, b_{II}), III (a_{III}, b_{III}), and IV (a_{IV}, b_{IV}) (The scale is 35 μm). (c) Schematic of locations of EBSD measurements. Black, red and blue lines indicate the high-angle, low-angle grain boundaries and Σ3 twinning boundaries, respectively. (For interpretation of the references to colour in this figure legend, the reader is referred to the Web version of this article.)

When the tensile strain increases to ~24 % and ~40 %, the forward martensitic transformation of $\gamma \rightarrow \alpha'$ appears to be heterogeneously reactivated at different locations (Fig. 6(b_2,b_3,c_2,c_3,d_2,d_3,e_2,e_3)). Specifically, the forward transformation at locations I and II occurs at strain levels <24 % (● ▲ in Fig. 6f), while at locations III and IV it happens mainly at higher strain stages >24 %. Notably, the extent of forward martensitic transformation (▼◆ in Fig. 6f) in the CT-30 sample (α' volume fraction70 %) exceeds that (~60.8 %) of the CG one (■ in Fig. 6f). This asynchronous occurrence, facilitated by the 3D-GGS, allows the martensitic transformation to endure a broader strain range, thereby enhancing high work hardening and ductility [34]. Moreover, the martensitic transformation at locations I and II occurs in the form of lamellas, creating a duplex-phase lamellar structure (Fig. 6(b_2,b_3,c_2,c_3)), which differs from the random occurrence observed at locations III and IV (Fig. 6(d_2,d_3,e_2,e_3)).

In addition to the phase composition illustrated in Fig. 6, shear bands (indicated by ellipses) can also be observed within γ austenite. For the CG sample, only a few shear bands emerge with tensile strain increasing from ~5.3 % to ~24 % (Fig. 6(a_1,a_2)). In contrast, for the CT-30 sample, abundant shear bands become activated and many intersections of shear bands are observed at locations III and IV (Fig. 6(d_1,d_2,e_1,e_2)) after tensile strain of ~5.3 % and ~24 %. Conversely, the density of shear bands at locations I and II of the CT-30 sample is relatively fewer (Fig. 5 (b_1,b_2,c_1,c_2)). The shear bands and their intersections can serve as the nucleating sites of α' martensite [41]. Consequently, the martensitic transformation of $\gamma \rightarrow \alpha'$ is significantly promoted at locations III and IV when the strain exceeds 24 % (▼◆ in Fig. 6d).

The EBSD KAM images and the corresponding mean GND densities for the CG and CT-30 samples after various tensile strains are presented in Fig. 7. For the CG sample (Fig. 7(a_1-a_3)), the KAM misorientation increases continuously with tensile strain, which is primarily caused by the strain partitioning between the softer γ austenite and the harder fresh α' martensite [42,46]. As a result, there is a persistent increase in the GND density (■ in Fig. 7f) and the HDI stress (■ in Fig. 4c). In contrast, the KAM misorientations at four locations of the CT-30 sample decrease first after a tensile strain of ~5.3 % (Fig. 7(b_1,b_1,c_1,d_1)), which can be due to the reverse transformation of $\alpha' \rightarrow \gamma$. As the tensile strain increases further, the KAM misorientation and GND density of the CT-30 sample begin to rise again (Fig. 7(b_2,b_3,c_2,c_3,d_2,d_3,e_2,e_3,f)). Significantly, the distributions of KAM misorientation at locations III and IV are highly in-homogeneous after a tensile strain of ~40 % (Fig. 7(d_3, e_3)), hinting at strong hetero-deformation. This is validated by the considerable fluctuation (from 0 to 3°) of KAM values observed in line measurements (Fig. 7g). In comparison, the CT-30 sample exhibits a higher GND density than the CG sample, devoting to the enhanced HDI stress (see Fig. 4), which is due to the collected effects of the 3D-GGS and the asynchronous martensitic transformation.

Fig. 8a plots representative HE XRD patterns taken along route i (i.e., thickness direction) of CT-processed 304ss during tensile deformation. It is evident that as the applied strain increases, the relative intensity of the γ peaks gradually declines while the α' peaks steadily intensify. This observation confirms the occurrence of forward martensitic transformation. Additionally, the positions of all peaks shift to lower 2θ values, indicating the lattice strain (ε_{hkl}) induced by stress, which can be determined by the formula [27,47,48], as follows:

$$\varepsilon_{hkl} = \frac{d_{hkl} - d^0_{hkl}}{d^0_{hkl}} \tag{1}$$

Where variables d^0_{hkl} and d_{hkl} represent the lattice spacing of the (hkl) plane before and during the tensile deformation, respectively, which can be obtained using the Bragg equation by measuring the positions of diffraction peaks integrated along the tensile direction (TD). However,

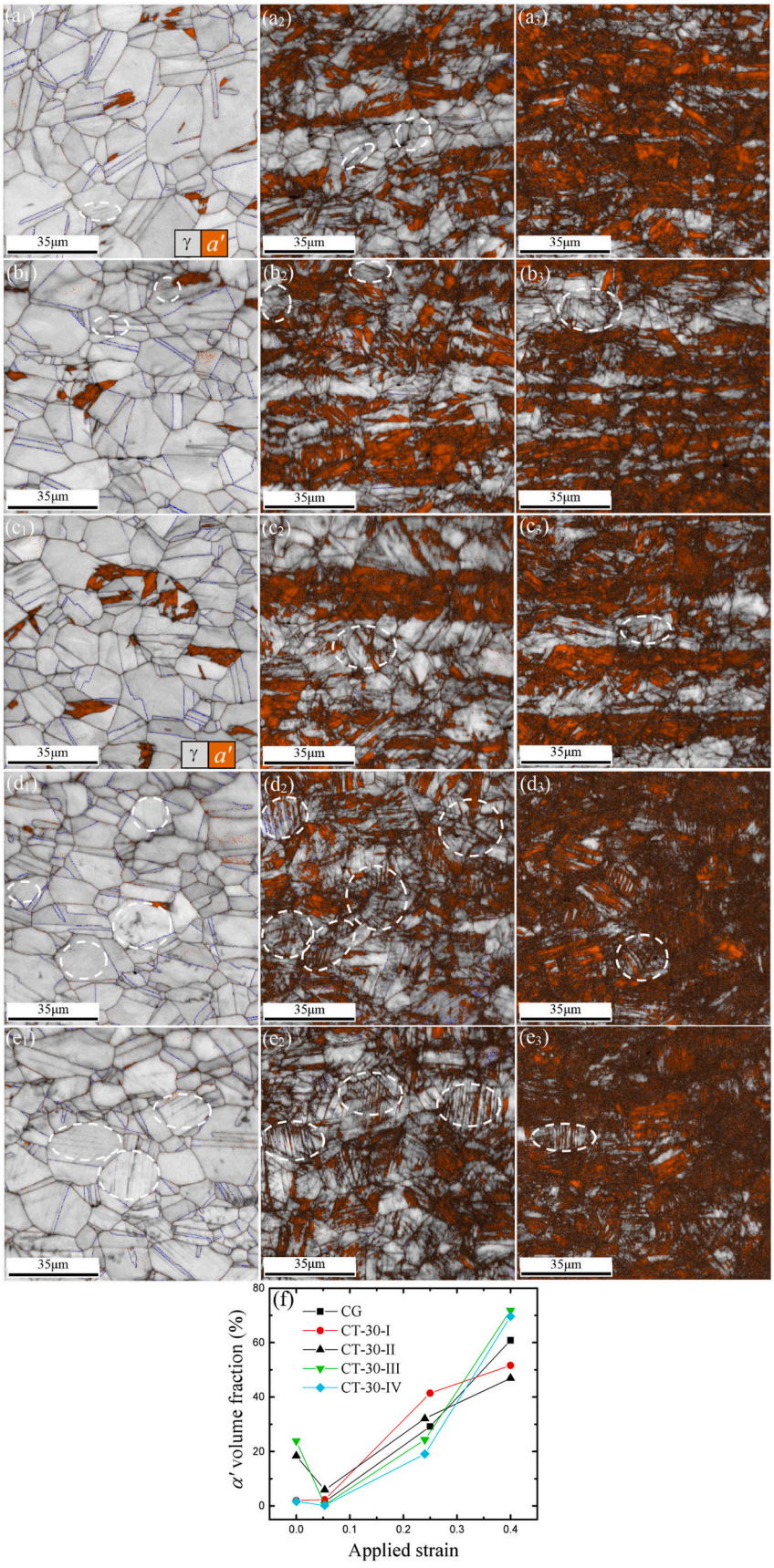

Fig. 6. Superimposed EBSD IQ plus phase images of CG (a) and (b–e) CT-30 304ss taken at locations I (b), II (c), III (d) and IV (e) after tensile strains of 5.3 % (b_1,c_1, d_1,e_1), 24 % (b_2,c_2,d_2,e_2) and 40 % (b_3,c_3,d_3,e_3). (f) Evolution of the volume fraction of α'-martensite of CG and CT-30 304ss at different locations with applied strain.

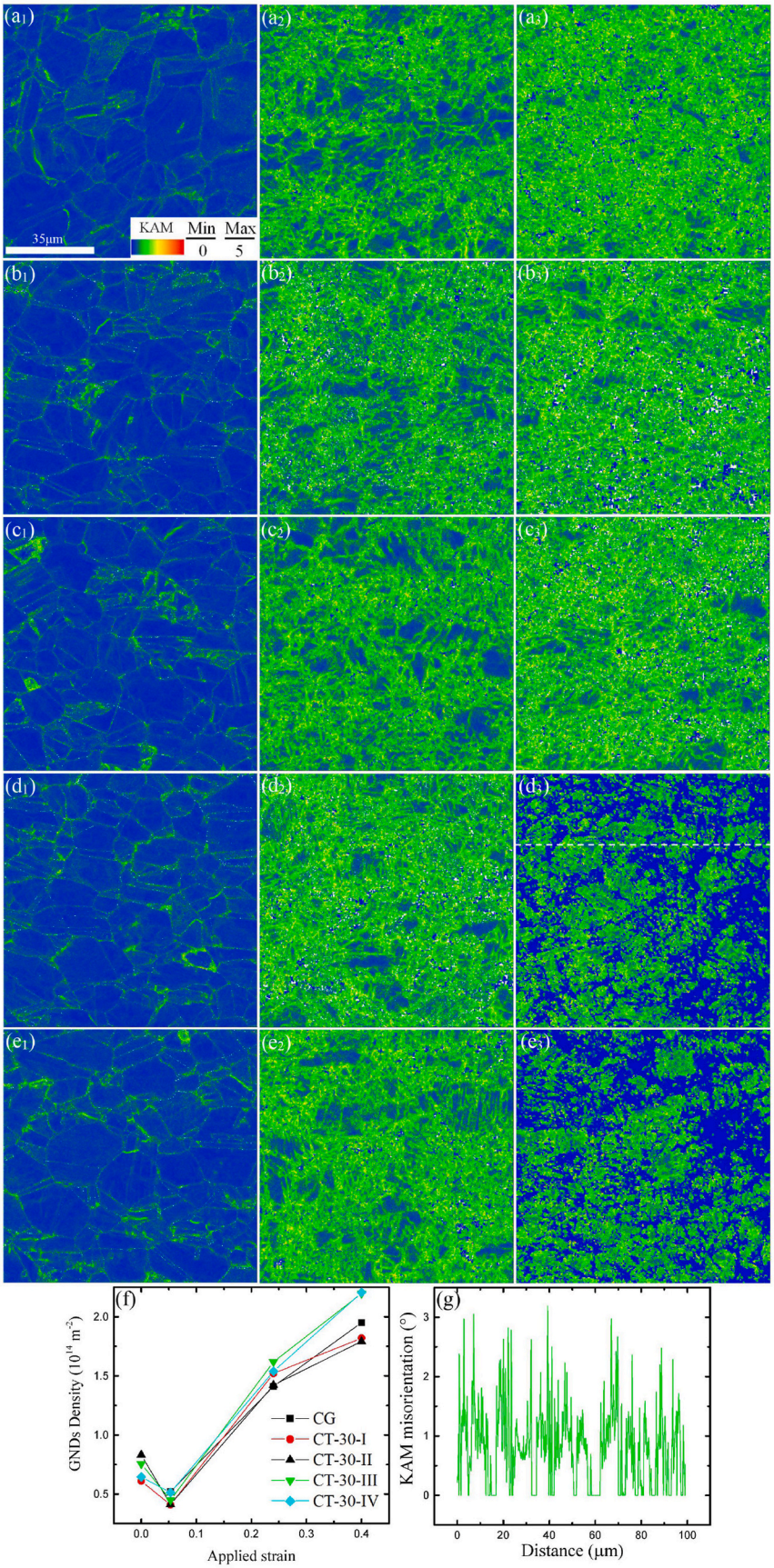

Fig. 7. (AZtec Crystal) EBSD KAM images of CG (a) and CT-30 (b,c,d,e) 304ss taken at locations I (b), II (c), III (d) and IV (e) after tensile strain of 5.3 % (a_1,b_1,c_1,d_1, e_1), 24 % (a_2,b_2,c_2,d_2,e_2) and 40 % (a_3,b_3,c_3,d_3,e_3). (f) Evolution of GNDs of the CG and CT-30 304ss at different locations with applied strain. (g) Line measurement of KAM of (d_3).

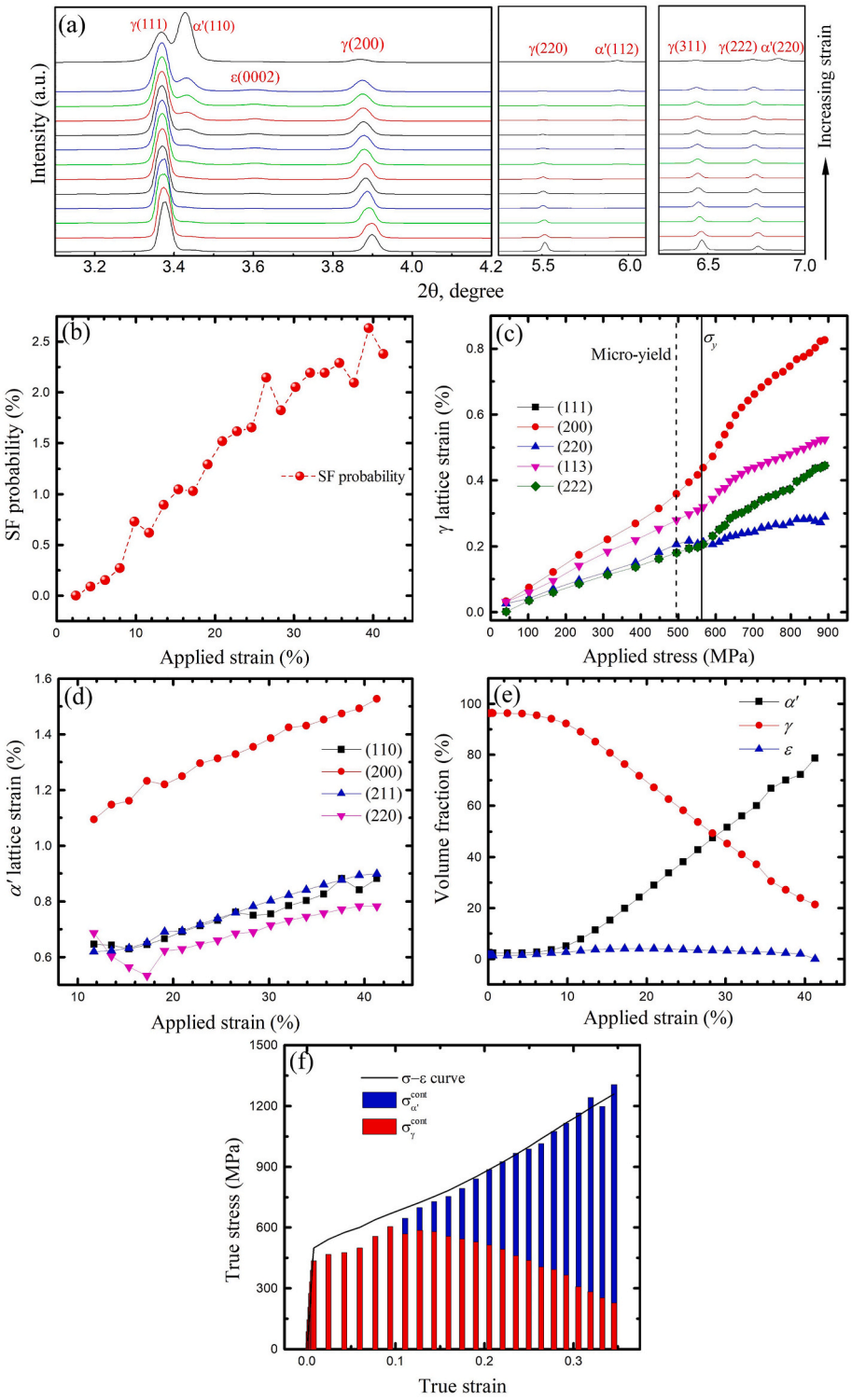

Fig. 8. (a) HE XRD spectrum, (b) SF probability versus applied strain, (c) γ lattice strain versus applied stress, (d) α' lattice strain versus applied strain, (e) Evolution of volume fraction of constituent phases with applied strain, (f) Phase stresses of γ austenite and α' martensite of CT-processed 304ss during tensile deformation.

except for applied stress, the formation of SFs can also affect the positions of γ peaks [49]. Therefore, it is important to first estimate the SF probability (P_{SF}) in γ austenite using the following method [48,50]:

$$p_{SF} = \frac{32\pi}{3\sqrt{3}}\left(\frac{d_{222}}{d_{222}^0} - \frac{d_{111}}{d_{111}^0}\right) \tag{2}$$

where d_{111}^0, d_{222}^0, d_{111}, d_{222} are the lattice spacing of (111) and (222) planes before and during the tensile deformation, respectively. The gradual increase in P_{SF} indicates that the density of SFs increases monotonously with the applied strain (Fig. 8b). Subsequently, the peak shifts caused by SFs can be evaluated for (111) and (222) planes by the following equations [48,50]:

$$\frac{\Delta d_{111}^{SF}}{d_{111}^0} = \frac{-\sqrt{3}P_{SF}}{16\pi} \tag{3}$$

$$\frac{\Delta d_{222}^{SF}}{d_{222}^{0}} = \frac{\sqrt{3} P_{SF}}{32\pi} \tag{4}$$

Finally, by eliminating the contribution of SFs, the elastic lattice strain caused by applied stress can be gained using the following method:

$$\varepsilon_{hkl}^{\sigma} = \frac{d_{hkl} - d_{hkl}^{0} - \Delta d_{hkl}^{SF}}{d_{hkl}^{0}} \tag{5}$$

Of course, the contribution of SFs to the peak shifts of α' martensite can be considered negligible. The evolution of lattice strains for different peaks under applied strain/stress in γ austenite and α' martensite are shown in Fig. 8(c and d). It is important to note that the lattice strains of ε martensite and the lattice strain of α' martensite at the low strain stage were not calculated due to the significant fitting errors of peak positions, which arise from their low peak intensities in TD and low volume fractions (Fig. 8e). When an applied stress is exerted, the lattice strains of all γ peaks increase in a linear manner (see Fig. 8c). However, before reaching the apparent yield stress, the lattice strains of (200) and (220) peaks deviate noticeably from the linear trend, indicating micro-yielding. This phenomenon can originate from the stress partitioning and load transfer between different zones at the elastic-plastic stage [45, 51]. In contrast, for α' martensite, a decrease in lattice strains of (110) and (220) peaks is observed within the strain ranges of 10 %–16 %, which may arise from the stress relaxation due to the pronounced martensitic transformation (Fig. 8e). Subsequently, the volume fraction of constituent phases is estimated using the following equation [48]:

$$f\alpha' = \frac{\frac{1}{n}\sum_{0}^{n} I_{\alpha'}^{hkl} \Big/ R_{\alpha'}^{hkl}}{\frac{1}{n}\sum_{0}^{n} I_{\alpha'}^{hkl} \Big/ R_{\alpha'}^{hkl} + \frac{1}{m}\sum_{0}^{m} I_{\gamma}^{hkl} \Big/ R_{\gamma}^{hkl} + \frac{1}{j}\sum_{0}^{j} I_{\varepsilon}^{hkl} \Big/ R_{\varepsilon}^{hkl}} \tag{6}$$

where $I_{\alpha'}^{hkl}$, I_{γ}^{hkl} and I_{ε}^{hkl} are the measured integrated intensity, $R_{\alpha'}^{hkl}$, R_{γ}^{hkl} and R_{ε}^{hkl} are theoretical integrated intensity with a completely random texture of α', γ and ε peaks, and n, m and j are the numbers of diffraction peaks for α', γ and ε phases, respectively. Diffraction peaks, integrated along all directions, are fitted to estimate the volume fraction of constituent phases. The results (Fig. 8e) indicate that the volume fraction of α' martensite increases from ~2.7 % to ~78.7 % as the tensile strain increases from ~6.0 % to ~41.3 %. This increase occurs alongside a continuous reduction in the volume fraction of γ austenite. Interestingly, the volume fraction of ε martensite first increases and then decreases during the tensile strain, although it remains pretty low, at 4.0 % or less.

Based on the measurements of lattice strains and volume fractions of constituent phases, the phase stresses of austenite (σ_{γ}^{count}) and martensite ($\sigma_{\alpha'}^{count}$) can be calculated using the following method [48]:

$$\sigma_{i}^{count} = \sum_{0}^{m} f_{i}^{hkl} E_{i}^{hkl} \varepsilon_{i-hkl}^{\sigma} \tag{7}$$

$$f_{i}^{hkl} = \frac{I_{i}^{hkl} / R_{i}^{hkl}}{\sum_{0}^{m} I_{i}^{hkl} / R_{i}^{hkl}} \tag{8}$$

where E_{i}^{hkl} and f_{i}^{hkl} are the elastic constant and volume fraction of <hkl>//TD grains within phase i, respectively. The phase stress of ε martensite can be disregarded, considering its low volume fraction ≤4.0 %. Notably, strong <111>//TD textures for γ austenite are observed at locations I and III after a tensile strain of ~40 % (see Fig. S9(a and c)). Accordingly, the phase stress of γ austenite is estimated from the lattice strain of <111>//TD grains, as detailed in a previous study [48]. When the texture is weak, the phase stress of α' martensite can be reliably assessed by averaging the lattice strain of <110>//TD, <211>//TD and <310>//TD grains [48]. For evaluating the phase stress of α' martensite in this study, two significant considerations must be made. First, a moderate <110>//texture is noted for strain-induced α' martensite at locations I and III after tensile strain of ~40 % (see Fig. S9(b and d)). Second, a considerable portion of (310) peak falls outside the detection range along the TD direction. Thus, a hypothesis is proposed where the phase stress of α' martensite is evaluated using the lattice strain of <110>//TD and <211>//TD grains, with an estimated percentage of these grains being about 80 %. The elastic constants for <111>//TD grains in γ austenite and for <110>//TD and <211>//TD grains in α' martensite are reported as 242 GPa, 194 GPa and 195 GPa, respectively, based on the work by Ref. [48], assuming the chemical composition of 304ss closely aligns with that discussed in their study. The calculated phase stresses for γ austenite and α' martensite are plotted in Fig. 8f, illustrating that the combined contributions of phase stresses of γ austenite and α' martensite coincides with the actual flow stress nicely. The contributed stress from α' martensite elevates monotonously along with the decreased stress from γ austenite, which can be due to the gradual forward transformation of $\gamma \rightarrow \alpha'$. This observation supports the notion that the stress/strain partitioning between γ austenite and α' martensite persists, contributing to the HDI work hardening.

TEM characterizations were performed to further investigate the microstructural evolution of 304ss sheets subjected to CT processing and subsequent tension. Shown in Fig. 9 are TEM images and selected area electron diffraction (SAED) patterns from location III of the CT-30 sample. The observations reveal the presence of annealing twins with parallel TBs measuring 3–5 μm in thickness, which is confirmed by the SAED pattern (Fig. 9(a–f)) and is consistent with the EBSD results (Fig. 5b). Nanoscale α'/ε bundles are observed, either parallel to TB or inclined at 60° to TB, induced in γ matrix from the martensitic transformation of $\gamma \rightarrow \varepsilon \rightarrow \alpha'$. Additionally, a few parallelepiped domains are formed after the CT processing (Fig. 9(a and b)). During the CT process, planar slips occurred, and dislocations piled up against grain boundaries and TBs, leading to the formation of sub-microscale dislocation cells (Fig. 9(a,b,d)). This behaviour is comparable to that observed in CT-processed high-entropy alloy [13,37]. Furthermore, α' martensite plates with sub-microscale thickness and microscale length are formed, nucleating from γ grain boundaries and triple junctions (Fig. 9(d and e)). These locations, which experience high-stress concentrations, facilitate the direct martensitic transformation of $\gamma \rightarrow \alpha'$ [52].

After ~5.3 % tensile strain in the CT-30 sample (Fig. 10), the volume fraction of α' martensite decreases considerably, which is consistent with the EBSD results showing the reverse transformation of $\alpha' \rightarrow \gamma$ (see Fig. 6 (c_1,f)). Instead, a substantial amount of SFs are formed in two slip directions (indicated by arrows in Fig. 10(a–d)), which is further confirmed by the additional diffraction fringes in SAED patterns (Fig. 10e). Many parallel ε martensite strips containing SFs with greater thickness are also noted (Fig. 10(b,c,f)). Additionally, (partial) dislocations are seen cutting through of ε strips, as indicated by triangles in Fig. 10c. High-density dislocations, referred to as GNDs, pile up at the γ grain boundaries, contributing to the HDI strain hardening (Fig. 4). Magnified TEM observations reveal that ultrafine SFs is activated with the intervals of around 100 nm (Fig. 10d).

As the tensile strain increases to ~24 % for the CT-30 sample, the dislocation density rises significantly (Fig. 11a), and enormous nano-scale α' bundles nucleating at SFs or ε strips (Fig. 11(b–d)) have been formed through the martensitic transformation of $\gamma \rightarrow \varepsilon \rightarrow \alpha'$. In addition, more secondary SFs and ε strips are produced between primary ε/α' bundles (Fig. 11(d and e)), resulting in a hierarchical structure of SFs and ε strips. The extensive formation of these SFs or ε strips facilitates the creation of α' martensite, which primarily develops within ε strips rather than at their intersections (Fig. 11(d,e,f)). The HRTEM results indicate that the thickness of ε/SFs ranges from 5 to 10 nm (Fig. 11g). The presence of SFs in both γ and ε phases is confirmed by the additional diffraction fringes seen in the FFT images (Fig. 11(h–k)). In contrast, no additional diffraction fringes are observed from the FFT images of γ

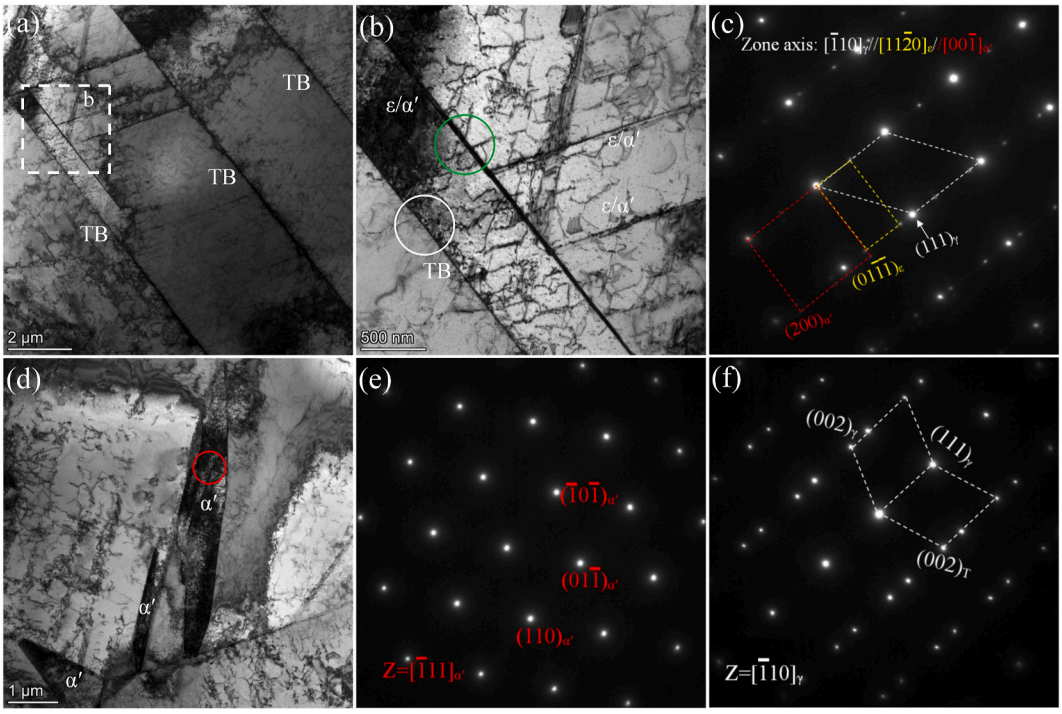

Fig. 9. TEM images and SAED patterns at location III in CT-30 304ss. (a) Bright field (BF) image highlighting the annealing twins and dislocation substructure, (b) Enlarged image of the region b delineated by the dot rectangle in (a), (c) SAED pattern taken from the martensite region indicated by the green ring in (b), (d) BF image highlighting the CT-induced α' martensite nucleating at γ grain boundaries, (e) SAED pattern taken from the α' martensite region indicated by the red ring in (d), (f) SAED pattern taken from the twin boundary (TB) indicated by the white ring in (b). (For interpretation of the references to colour in this figure legend, the reader is referred to the Web version of this article.)

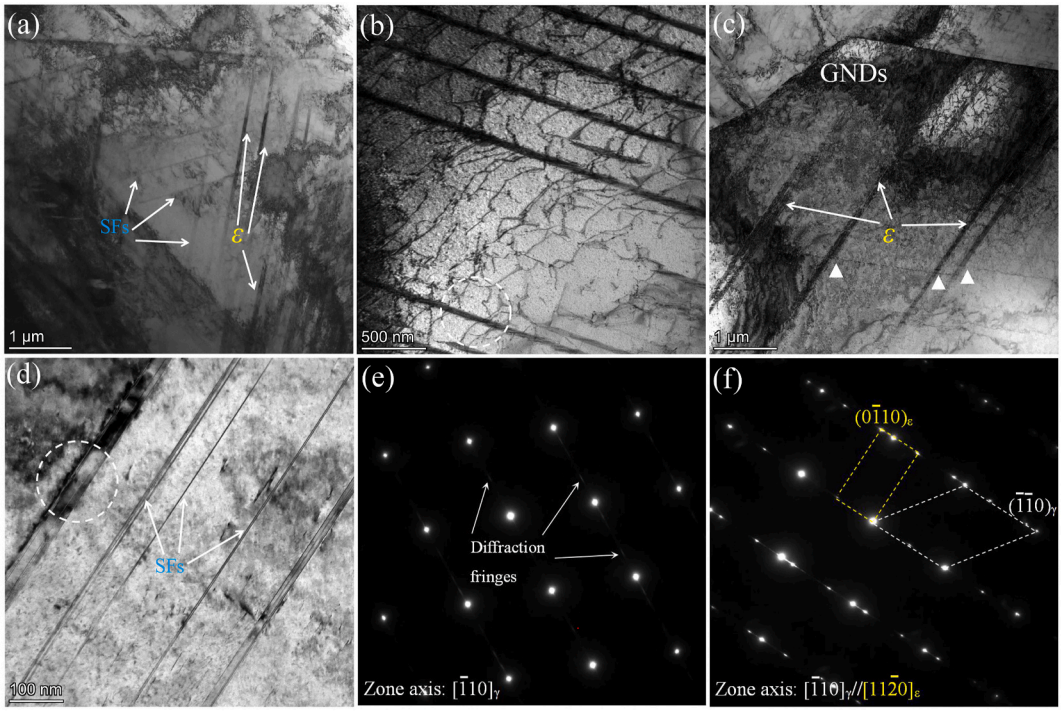

Fig. 10. TEM images and SAED patterns at location III in CT-30 304ss after tensile strain of 5.3 %. (a–d) BF images, (e,f) SAED patterns taken from the SFs region and ε strip region delineated by dot circles in (d) and (b), respectively. Arrows in (a,c,d) indicate the SFs and ε strips. Triangles in (c) show cutting through SFs by dislocations. Arrows in (e) indicate additional diffraction fringes from the SFs.

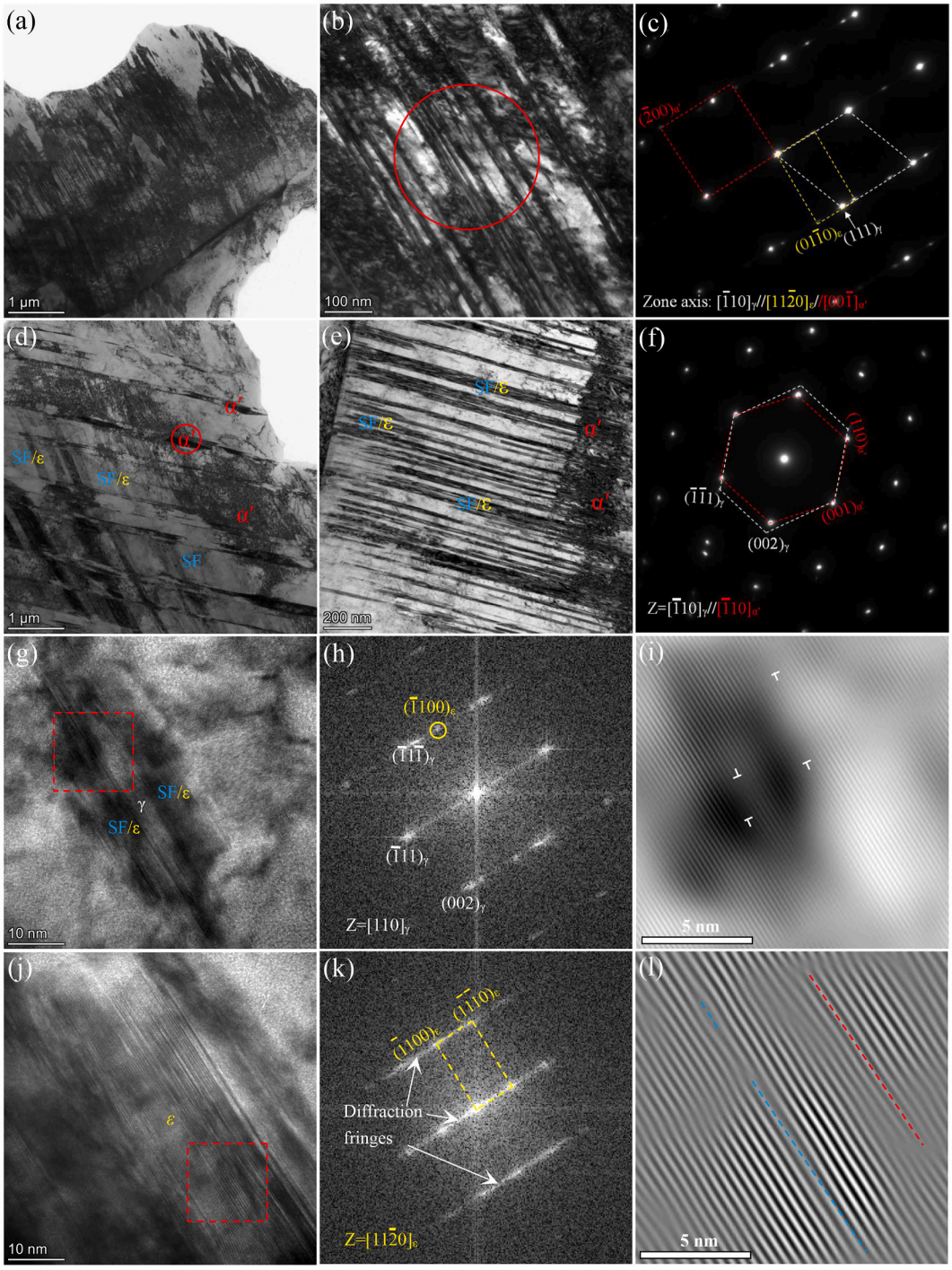

Fig. 11. TEM images and SAED patterns at location III in CT-30 304ss after tensile strain of ~24 %. (a) BF image highlighting the high-density dislocations and martensite bundles, (b) Enlarged image of (a), (c) SAED pattern taken from the region indicated by the red ring in (b), (d) BF image highlighting the hierarchical SFs/ε strips and α' plates, (e) Enlarged BF image of SFs/ε strips, (f) SAED pattern taken from the α' region indicated by the red ring in (d), (g) HRTEM image highlighting the SFs, (h) FFT pattern of the region delineated by the red quadrate in (g), (i) Inverse FFT image of (h), (j) HRTEM image highlighting the SFs in ε strips, (k) FFT pattern of the region delineated by the red quadrate in (j), (*l*) Inverse FFT image of (k). (For interpretation of the references to colour in this figure legend, the reader is referred to the Web version of this article.)

matrix without SFs (Fig. S10(a and b)). The FFT image (Fig. 11h) suggests that the SFs can be intrinsically HCP ε martensite embryos. The inverse FFT image reveals a significant number of dislocations present within the ε embryos (Fig. 11i). Furthermore, both the insertion-type SFs and the extraction-type SFs are observed in ε martensite through the FFT and inverse FFT images (Fig. 11(k,l) and S10 (c,d)). From the inverse FFT image of the γ austenite adjacent to SFs or ε strip (see Fig. S10), the estimated dislocation density is as high as ~1.9×10^{16} m^{-2}. This high density can be from the accumulations of moving dislocations that are impeded by SFs and ε strips [13,52,53].

To determine whether the reverse transformation of $\alpha' \rightarrow \gamma$ occurred during the tensile strain ranging from ~5.3 % to ~24 %, HRTEM observations were conducted at the phase interfaces between the α' and ε, as well as between the γ and ε. Fig. 12(a–c) display the HRTEM image of

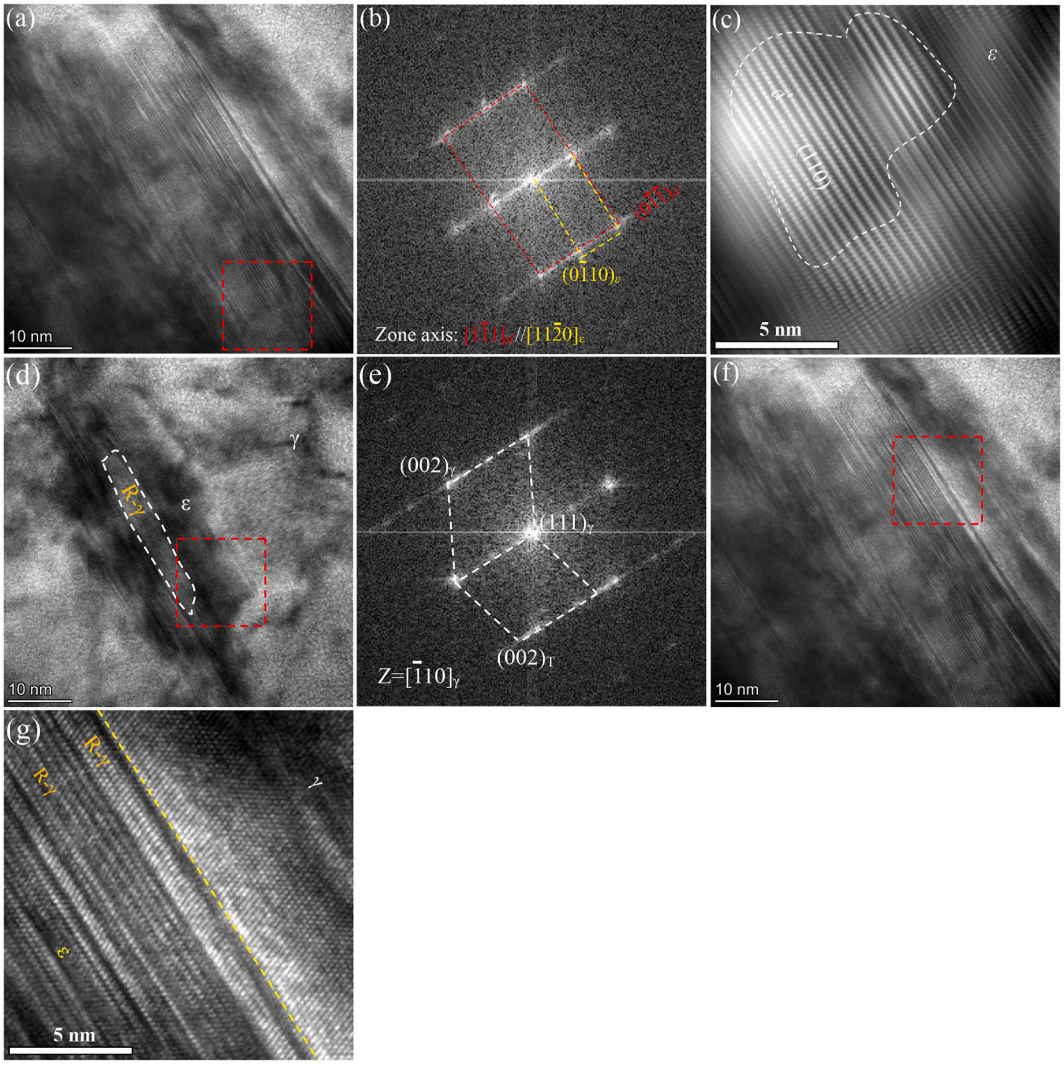

Fig. 12. (a) HRTEM images of a region comprised of α' and ε martensite at location III in CT-30 304ss after tensile strain of ~24 %, (b) FFT image and (c) inverse FFT image of (a), respectively. (d,f) HRTEM images of a region containing γ austenite, ε strip and reverted γ austenite (R-γ) at locations III in CT-30 304ss after tensile strain of 24 %, (e) FFT of red framed area in (d), (g) Inverse FFT of red framed area in (f). (For interpretation of the references to colour in this figure legend, the reader is referred to the Web version of this article.)

a region comprised of α' and ε martensite, which is validated by the presence of diffraction spots from both α' and ε martensite (Fig. 12b). The interface between the α' and ε martensite is visible in inverse FFT images, indicated by the white dot line in Fig. 12c. Notably, the reverted ε is gradually depleting α' martensite, providing evidence for the occurrence of the reverse transformation ($\alpha' \rightarrow \varepsilon$). Additionally, many SFs are observed within α' martensite (Fig. 12c), which can also facilitate the reverse transformation of $\alpha' \rightarrow \varepsilon$ [54].

A thin γ layer is observed to be enclosed by the ε strip, and a twin relationship between the γ matrix and the enclosed γ layer is confirmed by the SAED pattern (Fig. 12(d and e)). This observation validates the reverse martensitic transformation of $\varepsilon \rightarrow \gamma$, a phenomenon previously documented in stainless steel [55,56] and high-entropy alloy [17,43]. Fig. 12(f and g) show the HRTEM and inverse FFT images of the interface between ε martensite and γ austenite. Within ε martensite, the reverted γ embryos can be seen, and the γ austenite gradually extends into ε martensite, providing strong evidence for the reverse transformation of $\varepsilon \rightarrow \gamma$. Also, many SFs are present in ε martensite (Fig. 12g), which facilitates the reverse transformation of $\varepsilon \rightarrow \gamma$. Based on the above HRTEM observations, it can be deduced that the reverse transformation of $\alpha' \rightarrow \gamma$ occurs with ε serving as an intermediate phase, outlining the reverse processes of $\gamma \rightarrow \varepsilon \rightarrow \alpha'$.

When the tensile strain reaches ~40 %, the volume fraction of α' martensite with high-density dislocations increases prominently (Fig. 13 (a,b,c)). This observation is consistent with the EBSD results (see Fig. 6 (d–f)). The prior annealing TBs are disrupted due to the interaction between the TBs and the martensitic transformation (Fig. 13a). The starlike diffraction spots indicate high internal stress, which arises from the volume expansion of α' martensite during the forward martensitic transformation process (Fig. 13d). Enlarged TEM observations reveal that lamellar and block-shape ultrafine γ austenite are still retained with comparatively fewer dislocations (Fig. 13(b and c)). Furthermore, nanoscale mechanical twinning is activated alongside the ε/α' martensite (Fig. 13(e and f)), which can be assisted by high flow stress. In conclusion, the sustained martensitic transformation of $\gamma \rightarrow \alpha'$, along with the activation of mechanical nanotwinning, contributes to the work hardening and uniform deformation of the CT-30 sample at high strain levels [38,57].

3.3. Discussion

3.3.1. Characteristics of novel 3D-GGS in 304ss sheets

Previous studies have demonstrated that both unidirectional and cyclic twisting techniques can be used to tailor GGS structures in metal

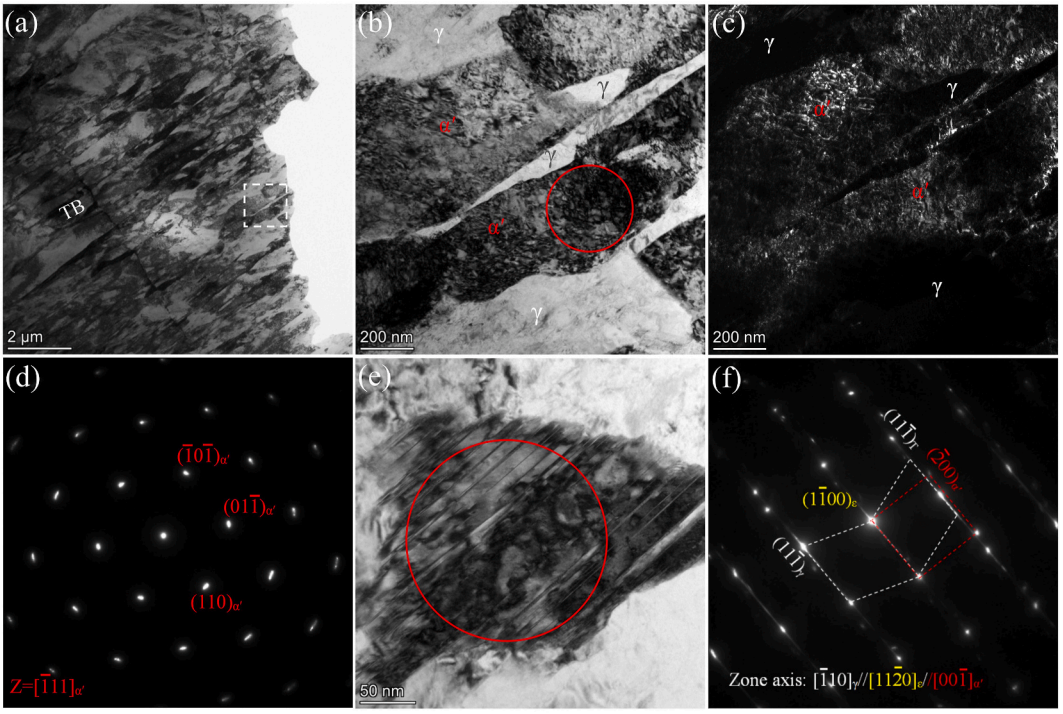

Fig. 13. TEM images and SAED patterns at location III in CT-30 304ss after tensile strain of ~40 %. (a) BF image highlighting the numerous α' martensite, (b) Enlarged image of the region delineated by the white quadrate in (a), (c) Dark field image of (b), (d) SAED pattern taken from the α' martensite region indicated by the red ring in (b), (e) Enlarged BF image highlighting the nanotwins and martensite, (f) SAED pattern taken from the region indicated by the red ring in (e). (For interpretation of the references to colour in this figure legend, the reader is referred to the Web version of this article.)

rods [13,38–40]). The equivalent strain (ε) induced by twisting in metal rods can be expressed in its simplest form as follows [40]:

$$\varepsilon = r\frac{\theta}{\sqrt{3}l_0} \tag{9}$$

Where θ is the twist angle, r is the radius, and l_0 is the length of a rod, respectively. For a certain θ, the plastic strain increases linearly with increasing radius from core to surface. Consequently, global gradient-dislocation structures have been developed using CT processing in high-entropy alloy and stainless steel rods [13,38,52,58]. Notably, the microstructural and *Hv* measurements at a specific radius across different directions have been shown to be nearly identical for metal rods subjected to unidirectional twisting and CT processing [13,38,59]. Unexpectedly, the *Hv* and EBSD results (see Figs. 2 and 5) suggest that formula (9) can no longer be applicable for estimating the strain distribution of CT-processed metal sheets. The deformation physics at the cross-section of a metal sheet during CT processing is more complicated, likely due to the mutual constraints between different sample zones. The formation of the novel 3D-GGS is closely linked to the specific stress/-strain states at the cross-section of 304ss sheets during the CT processing. This aspect can be influenced by the width-to-thickness ratio of a sheet and various CT parameters (e.g., CT rate, angle amplitude and cyclic passes).

Additionally, it is important to note that 304ss sheets of a different gauge geometry (10 × 3 × 2 mm^3) were utilized to conduct the in-situ HE X-ray studies. The decision to use 15 cycles instead of 60 cycles is primitively based on formula (9) to obtain the purportedly similar 3D-GGS as in the CT-30 sample, considering that the gauge length (10 mm) is reduced to a quarter of the original size (40 mm). Fortunately, the engineering stress-strain curve of the CT-processed 304ss sheet used for HE XRD studies (see Fig. 8f) closely resembles that of the CT-30 sample (see #4 in Fig. 1a). Future experimental and simulation studies will help elucidate the formation mechanism of the novel 3D-GGS in

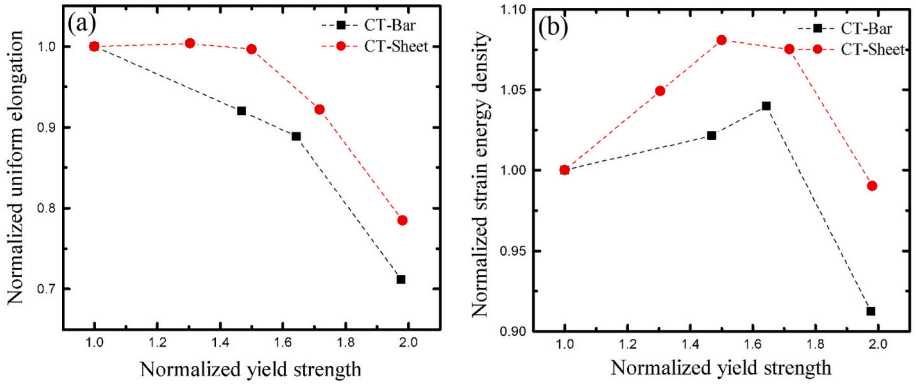

Fig. 14. Comparison of normalized uniform elongation versus normalized yield strength (a) and normalized strain energy density versus normalized yield strength (b) between 3D-GGS 304ss sheets and GGS 304ss rods [58].

metal sheets.

Fig. 14 compares normalized mechanical properties between 3D-GGS 304ss sheets and GGS 304 rods [58], relative to their CG samples. The results indicate that 3D-GGS 304ss sheets achieve significantly better combinations of strength, ductility and toughness compared to GGS 304ss rods. This enhancement can be attributed to the increased structural heterogeneity and zone boundaries present in 3D-GGS sheets, which enhance HDI strengthening and strain hardening [4]. Therefore, one key advantage of the CT processing technique is its ability to create greater structural heterogeneity and to improve overall performance by producing 3D-GGS in metal sheets. Additionally, this technique offers the potential to enhance the integrated mechanical properties of structures at a low cost, without altering their geometries.

3.3.2. Strengthening mechanisms

As presented in Fig. 1, the yield strength of CT-treated 304ss sheets progressively increases with the CT angle amplitude, ranging from ~10° to ~50°. Characterizations using EBSD and TEM (see Figs. 5 and 9 and S2), along with the *Hv* distribution at the cross-section (Fig. 2), clearly reveal the development of a novel 3D-GGS, which arises from both the dislocation density and the α'-martensite content gradients. Additionally, the novel 3D-GGS features multiple zone boundaries (Fig. 15a). Consequently, the introduction of large amounts of dislocations (referred to as dislocation strengthening) and harder ε/α' martensite (known as precipitation strengthening) contribute to the improved yield strength of the CT-30 304ss. However, the direct contribution of martensitic strengthening may be minor due to the low volume fraction <3.0 % (see Fig. 8e). Furthermore, it is suggested that both the dislocation density and the volume fraction of α' martensite elevate with a higher the CT angle amplitude, which ultimately leads to the gradual enhancement in yield strength (see Fig. 1a).

In addition to conventional strengthening mechanisms, HDI strengthening has been identified as a significant factor contributing to the increased strength of heterostructured materials [4,7]. In the case of 3D-GGS structure, there are two levels of mechanical incompatibility during the elastic-plastic deformation stage. These include the macroscopic mechanical incompatibility between soft zones (e.g., locations I and IV) and hard zones (e.g., locations II and III), as well as microscopic mechanical incompatibility between γ austenite and α' martensite. These mechanical incompatibilities must be accommodated by piling up GNDs near zone boundaries, resulting in a high HDI stress (>300 MPa) (see Fig. 4). When compared to the CG sample, the increased HDI stress ($\Delta\sigma_{HDI}$~119 MPa) accounts for ~61.3 % of the total yield strength increment ($\Delta\sigma_y$~194 MPa) observed in the CT-30 sample. This clearly indicates that the HDI strengthening is a major contributor to the increase in the yield strength of the 3D-GGS 304ss sheets. Furthermore, when compared to the global gradient dislocation structure in 304ss rods [58], the 3D-GGS in the 304ss sheets exhibits greater heterogeneity and a more pronounced heterostructural effect, which is responsible for their superior strength-ductility combinations (see Fig. 14).

3.3.3. Toughening mechanisms

In austenitic stainless steels, the deformation mechanism is determined by the mechanical stability of the γ austenite and arises from the mutual competition between dislocation slip and martensitic transformation [60,61]. Recent studies have unveiled new deformation mechanisms in heterostructured austenitic stainless steel that exhibit exceptional combinations of strength and ductility. For instance, in gradient nano-grained 301 and 304 stainless steels, the martensitic transformation of $\gamma \rightarrow \alpha'$ occurs earlier and extends over a wider range of plastic strain [34,35]. This transformation is significantly promoted by the high HDI stress or stress concentration in the gradient nano-grained 316 L stainless steel, gradient dislocation structured 304ss and heterogeneous lamellar-structured stainless steel [62–65]. Additionally, recent findings have revealed the co-activation of mechanical twinning and martensitic transformation in gradient dislocation-structured and heterogeneous lamellar structured austenitic stainless steels [38,65]. Combining heterostructures with martensitic transformation enables the HDI work hardening to persist over large strain range exceeding 20 % [17,38].

The 3D-GGS 304ss exhibits novel deformation mechanisms, including the reverse martensitic transformation, heterogeneous forward martensitic transformation and sustained HDI work hardening. These mechanisms are illustrated in a schematic diagram (Fig. 15) that outlines their relation to tensile strain. Notably, the reverse martensitic transformation of preexisting α' martensite into ε martensite and finally into γ austenite occurs unexpectedly at low strains under 5.3 % (see Figs. 6 and 10). It is significant that such a large volume fraction of reverse transformation of $\alpha' \rightarrow \gamma$ (from ~23.9 % to ~0.5 %) at room temperature is reported for the first time in austenitic stainless steel. This phenomenon contrasts with earlier findings on SMAT-treated 304ss, where reverse transformation was attributed to heat effects in

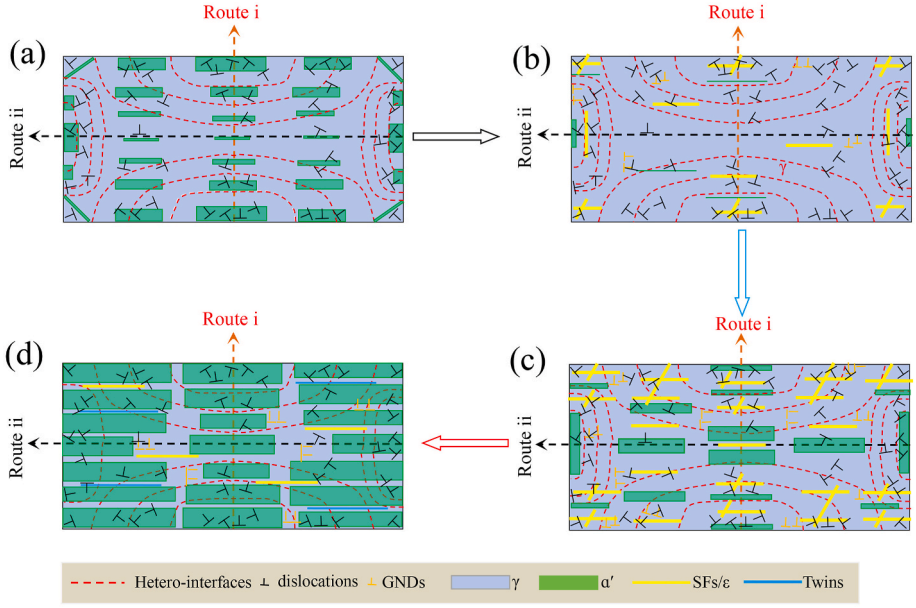

Fig. 15. Schematic of evolution of 3D-GGS during tensile strain of (a) 0 %, (b) 5.3 %, (c) 24 % and (d) 40 %.

shear bands [34]. Earlier studies have reported that when austenitic steels undergo partial martensitic transformation, the retained austenite becomes more stable and is less likely to transform into martensite [60]. Consequently, the reverted γ austenite formed by reverse transformation can subsequently transform back into α' martensite again (i.e., forward martensitic transformation) during the further tensile deformation. Importantly, the reverse transformation can lower the stability of retained γ austenite after CT processing, thereby facilitating the forward martensitic transformation. The unique TRIP effect, involving reverse and subsequent forward martensitic transformation, can lead to higher ductility. Additionally, reverse transformation of $\varepsilon \rightarrow \gamma$ has also been documented in the high-entropy alloys [44,54,65], duplex steel [66] and austenitic steel [55,56]. Sequential bidirectional transformations have been reported to be linked with superior work hardening and strength-ductility combinations in high-entropy alloys [17,43–45]). In the 3D-GGS 304ss, the reverse martensitic transformation of $\alpha' \rightarrow \gamma$ can be partially due to low SF energy that promotes the activation of partial dislocations and SFs (Fig. 10). In addition, the transition in stress state from CT to tension likely play a critical role in promoting the reverse motion of partial dislocations and stimulating the reverse transformation of $\alpha' \rightarrow \gamma$. High stress partitioning at harder zones (i.e., locations II and III) during tensile strain can also serve as an extra driving force for this reverse transformation. Olson and Cohen proposed that the martensitic transformation of bcc → fcc might be accomplished by the Bogers-Burgers fcc → bcc mechanism in reverse assisted by faulting [54], a concept supported by in-situ observations in Au-Cd alloy [67]. Our HRTEM observations (Figs. 10 and 12) prove the reverse martensitic transformation via $\alpha' \rightarrow \varepsilon \rightarrow \gamma$, representing the reverse process of the Bogers-Burgers-Olson-Cohen fcc → bcc mechanism. To further investigate whether the reverse transformation occurred in the 3D-GGS 304ss sheets at the high strain stage, detailed EBSD analyses were executed at location III after the tensile strain of ~40 %, as depicted in Fig. S12a. Numerous submicron γ islands are identified within α' martensite matrix, which can be either untransformed γ or reverted γ austenite. Fig. S12(b_1,b_2) indicate that some submicron γ islands are misaligned by 60°, indicating a twinning relationship with the γ austenite matrix (from point A to point B and from point C to point D). This observation suggests the formation of reverted γ austenite and affirms the presence of reverse transformation, similar to findings in high-entropy alloys [44,45,54]. The persistent reverse transformation at location III in the 3D-GGS 304ss sheets is likely associated with the continuously increased forward stress, which can contribute to overcoming the relatively high energy barriers between the γ austenite, ε and α' martensite. In effect, the reverse transformation of $\alpha' \rightarrow \varepsilon \rightarrow \gamma$ can relieve and accommodate the stress and strain field generated by forward transformation [17,65]. Thus, the sustained interplay of reverse and forward martensitic transformations is crucial for achieving the higher ductility seen in the 3D-GGS 304ss sheets.

The heterogeneous forward martensitic transformation of $\gamma \rightarrow \alpha'$ in the 3D-GGS 304ss sheets is evident under the applied strains (Fig. 6). Specifically, the early activation occurs at softer locations I and IV, while later induction is noted in harder locations II and III, allowing the martensitic transformation to persist across an extensive strain range (from ~5.3 % to >40 %). This behavior is comparable to that seen in gradient nanograined 304ss [34]. Furthermore, the forward martensitic transformation is further promoted at locations III and IV, assisted by numerous shear bands, SFs and ε strips (Figs. 6, 10 and 11), along with high-stress conditions. Besides, lamellar α' martensite appears at locations I and II (Fig. 6(b_2,b_3,c_2,c_3)), contributing to the formation of a γ/α' dual-phase lamella microstructure. Therefore, the persisted and promoted forward martensitic transformation, along with the formation of γ/α' dual-phase lamella microstructure, facilitates the dynamical Hall-Petch effect, high strain hardening and improved uniform elongation [34,35,43,58,63,68]. Furthermore, the enormous transformation of α' martensite primarily occurs within one ε martensite plate (Fig. 11) rather than the intersection of two ε martensite plates, which can result from the fact that the existence of SFs in strain-induced ε martensite (Fig. 11(g–j,k,l) and S10 (c,d)) can match the shear of a $\frac{T}{3}$ partial dislocation array [54,65]. To accommodate the $\varepsilon \rightarrow \alpha'$ transformation strain, some partial dislocations can reside at the interface between the ε and α' martensite [65]. These (retransformation) partial dislocations at phase interfaces can become mobile and locally push the α' retransforming into ε martensite and finally into γ austenite to relieve partial internal transformation strains. Therefore, it can be drawn that the forward ($\gamma \rightarrow \alpha'$) and reverse transformation ($\alpha' \rightarrow \gamma$) can occur concurrently at high strain ranges. The amplitude of the forward transformation surpasses that of the reverse transformation, resulting in a higher volume fraction of α' martensite.

The 3D structural heterogeneity (Fig. 5), the dynamical strain partitioning during martensitic transformation (Figs. 6 and 8f) and the late activation of mechanical nanotwinning (Fig. 13e,f) can all contribute to the persistent 3D strain gradient and piling up of GNDs [20,22,30,68,66]. The accumulation of GNDs, along with the interaction of GNDs and mobile dislocations, enhances the storage of dislocations and promotes forest hardening [4,69]. Importantly, the steady piling up of GNDs also leads to significant HDI work hardening, which persists throughout the whole uniform plastic deformation stage (see Fig. 4). As indicated in Fig. 8e, the volume fraction of α' martensite rises significantly when the applied strain exceeds 10 %. Therefore, at true strain ~0.15, the significant increase in the HDI stress can arise from the collected contribution of the 3D-GGS and the martensitic transformation, i.e., dynamical strain partition. Clearly, the sustained HDI work hardening plays a vital role in maintaining the high strain hardening and ductility of 3D-GGS 304ss sheets.

4. Conclusions

The mechanical properties and microstructures before and after tensile deformation of 304 stainless steel sheets processed by cyclic twisting have been investigated in detail. The following conclusions can be drawn:

(1) A novel 3D-GGS was successfully developed using cyclic twisting (CT) processing, resulting in a superior strength-ductility combination in 304ss sheets.
(2) The enhanced strength is attributed to the introduction of numerous dislocations, the formation of α' martensite and the increased HDI strengthening associated with the novel 3D-GGS.
(3) The high ductility could be explained by the multi-stage work hardening behaviors triggered by multiple deformation mechanisms. Specifically, the reverse martensitic transformation ($\alpha' \rightarrow \gamma$), forward martensitic transformation ($\gamma \rightarrow \alpha'$) and nanotwinning were heterogeneously induced at different zones and under varying strain conditions. Furthermore, the combination of the 3D-GGS, martensitic transformation and nanotwinning facilitated the sustained HDI work hardening through the uniform plastic deformation stage.
(4) This study offers valuable insights into the architecture of novel 3D-GGS structures and highlights the synergistic enhancement of strength and ductility of metal sheets. It also proposes an effective strategy for optimizing the integrated mechanical properties of components at a low cost without altering their geometries.

CRediT authorship contribution statement

Yindong Shi: Writing – review & editing, Writing – original draft, Funding acquisition. **Aojie Zhang:** Investigation, Data curation. **Lina Wang:** Methodology, Investigation. **Tao Liu:** Methodology, Investigation. **Xiliang Zhang:** Writing – review & editing, Funding acquisition. **Xinrui Yang:** Investigation. **Zhenguo Xing:** Methodology. **Yuntian**

Zhu: Writing – review & editing, Funding acquisition.

Declaration of competing interest

The authors declare that they have no known competing financial interests or personal relationships that could have appeared to influence the work reported in this paper.

Acknowledgments

This work is supported by the National Key R&D Program of China (2021YFA1200202), the National Natural Science Foundation of China (No. 11847130, 51874114), and the Hebei Natural Science Foundation (No. E2024402023, E2024402012). We also appreciate R. Zhou and J. Yan for fruitful discussion on experimental analysis. The synchrotron X-ray diffraction experiments were performed at DESY P21.1 High Energy X-Ray Diffraction for Physics and Chemistry at the Swedish Beamline.

Appendix A. Supplementary data

Supplementary data to this article can be found online at https://doi.org/10.1016/j.msea.2025.148383.

Data availability

Data will be made available on request.

References

[1] Y. Zhu, K. Ameyama, P.M. Anderson, I.J. Beyerlein, H. Gao, H.S. Kim, E. Lavernia, S. Mathaudhu, H. Mughrabi, R.O. Ritchie, N. Tsuji, X. Zhang, X. Wu, Heterostructured materials: superior properties from hetero-zone interaction, Mater. Res. Lett. 9 (2021) 1–30.
[2] X. Zhang, Heterostructures: new opportunities for functional materials, Mater. Res. Lett. 8 (2020) 49–59.
[3] H.-T. Zhang, T. Zhang, X. Zhang, Perspective and prospects for ordered functional materials, Adv. Sci. 10 (2023) 2300193.
[4] Y. Zhu, X. Wu, Heterostructured materials, Prog. Mater. Sci. 131 (2023) 101019.
[5] Y. Hua, X. Li, J. Li, X. Luo, Y. Li, W. Qin, L. Zhang, J. Xiao, W. Xia, P. Song, M. Yue, H.-T. Zhang, X. Zhang, Fast fabrication of a hierarchical nanostructured multifunctional ferromagnet, Science 385 (2024) 634–641.
[6] W. Ji, R. Zhou, P. Viveganandhan, M.S. Wu, H. Gao, K. Zhou, Recent progress in gradient-structured metals and alloys, Prog. Mater. Sci. 140 (2023) 101194.
[7] X.L. Wu, M.X. Yang, F.P. Yuan, G.L. Wu, Y.J. Wei, X.X. Huang, Y.T. Zhu, Heterogeneous lamella structure unites ultrafine-grain strength with coarse-grain ductility, Proc. Natl. Acad. Sci. USA 112 (2015) 14501–14505.
[8] J.S. Li, Y. Cao, B. Gao, Y.S. Li, Y.T. Zhu, Superior strength and ductility of 316L stainless steel with heterogeneous lamella structure, J. Mater. Sci. 53 (2018) 10442–10456.
[9] C.X. Huang, Y.F. Wang, X.L. Ma, S. Yin, H.W. Höppel, M. Göken, X.L. Wu, H.J. Gao, Y.T. Zhu, Interface affected zone for optimal strength and ductility in heterogeneous laminate, Mater. Today 21 (2018) 713–719.
[10] X.L. Ma, C.X. Huang, J. Moering, M. Ruppert, H.W. Höppel, M. Göken, J. Narayan, Y. Zhu, Mechanical properties in copper/bronze laminates: role of interfaces, Acta Mater. 116 (2016) 43–52.
[11] G. Huang, X. Li, L. Lou, Y. Hua, G. Zhu, M. Li, H.-T. Zhang, J. Xiao, B. Wen, M. Yue, X. Zhang, Engineering bulk, layered, multicomponent nanostructures with high energy density, Small 14 (2018) 1800619.
[12] T.H. Fang, W.L. Li, N.R. Tao, K. Lu, Revealing extraordinary intrinsic tensile plasticity in gradient nano-grained copper, Science 331 (2011) 1587–1591.
[13] Q. Pan, L. Zhang, R. Feng, Q. Lu, K. An, A.C. Chuang, J.D. Poplawsky, P.K. Liaw, L. Lu, Gradient-cell–structured high-entropy alloy with exceptional strength and ductility, Science 374 (2021) 984–989.
[14] X. Li, L. Lou, Y. Li, G. Zhang, Y. Hua, W. Li, H.-T. Zhang, M. Yue, X. Zhang, Macroscopic gradient ordered α-Fe/$Pr_2Fe_{14}B$ nanocomposites with ultrahigh energy density, Nano Lett. 22 (2022) 7644–7650.
[15] L. Lou, Y. Li, X. Li, H. Li, W. Li, Y. Hua, W. Xia, Z. Zhao, H. Zhang, M. Yue, X. Zhang, Directional magnetization reversal enables ultrahigh energy density in gradient nanostructures, Adv. Mater. 33 (2021) 2102800.
[16] H. Li, X. Li, D. Guo, L. Lou, W. Li, X. Zhang, Three-dimensional self-assembly of core/shell-like nanostructures for high-performance nanocomposite permanent magnets, Nano Lett. 16 (2016) 5631–5638.
[17] G. Yang, J.-K. Kim, Hierarchical precipitates, sequential deformation-induced phase transformation, and enhanced back stress strengthening of the micro-alloyed high entropy alloy, Acta Mater. 233 (2022) 117974.
[18] X. Li, L. Lou, W. Song, G. Huang, F. Hou, Q. Zhang, H. Zhang, J. Xiao, B. Wen, X. Zhang, Novel bimorphological anisotropic bulk nanocomposite materials with high energy products, Adv. Mater. 29 (2017) 1606430.
[19] X. Li, L. Lou, W. Song, Q. Zhang, G. Huang, Y. Hua, H. Zhang, J. Xiao, B. Wen, X. Zhang, Controllably manipulating three-dimensional hybrid nanostructures for bulk nanocomposites with large energy products, Nano Lett. 17 (2017) 2985–2993.
[20] Y. Zhou, K. Wang, X. Wen, R. Xin, J. Wang, Q. Liu, Achieving combination enhancement of strength and ductility in Ti-6Al-2Sn-4Zr-2Mo-0.1Si alloy by fabricating a new multiscale microstructure, Scr. Mater. 226 (2023) 115233.
[21] X. Geng, J. Gao, Y. Huang, S. Wang, Y. Zhang, G. Wu, H. Zhao, H. Wu, X. Mao, A novel dual-heterogeneous-structure ultralight steel with high strength and large ductility, Acta Mater. 252 (2023) 118925.
[22] D. Li, G. Fan, X. Huang, D.J. Jensen, K. Miao, C. Xu, L. Geng, Y. Zhang, T. Yu, Enhanced strength in pure Ti via design of alternating coarse- and fine-grain layers, Acta Mater. 206 (2021) 116627.
[23] Y. Wang, X. Ma, F. Guo, Z. Zhao, C. Huang, Y. Zhu, Y. Wei, Strong and ductile CrCoNi medium-entropy alloy via dispersed heterostructure, Mater. Des. 225 (2023) 111593.
[24] J. Nie, Y. Chen, X. Chen, X. Liu, Y. Zhu, Stiff, strong and ductile heterostructured aluminum composites reinforced with oriented nanoplatelets, Scr. Mater. 189 (2020) 140–144.
[25] X.D. Sun, X. Sun, X. Hao, J. Nie, Y. Fan, Y. Chen, S. Liu, X. Liu, Y. Zhao, Microstructure and enhanced cryogenic tensile property of a heterostructured Al-AlN/Al-Mg composite fabricated by accumulative roll bonding (ARB), J. Mater. Res. Technol. 21 (2022) 532–545.
[26] X. Sun, Y. Fan, J. Nie, Y. Chen, K. Xie, S. Liu, Y. Zhao, X. Liu, Significant improvement of the room and cryogenic mechanical properties of an AlN particle reinforced Al matrix composite by alloying element magnesium, Compos. Part B-Eng. 268 (2024) 111056.
[27] M. Jiang, Y. Wu, J. Nie, Y. Chen, Y. Fan, X. Liu, Y. Zhao, Revealing the ultra-high high-temperature compressive mechanical properties and deformation mechanism of a heterostructured AlNp/Al nanocomposite, Mater. Sci. Eng. A 878 (2023) 145199.
[28] J. Nie, Y. Chen, L. Song, Y. Fan, Y. Cao, K. Xie, S. Liu, X. Liu, Y. Zhao, Y. Zhu, Enhancing strength and ductility of Al-matrix composite via a dual-heterostructure strategy, Int. J. Plast. 171 (2023) 103825.
[29] Y. Zhu, X. Wu, Perspective on hetero-deformation induced (HDI) hardening and back stress, Mater. Res. Lett. 7 (2019) 393–398.
[30] M. Yang, Y. Pan, F. Yuan, Y. Zhu, X. Wu, Back stress strengthening and strain hardening in gradient structure, Mater. Res. Lett. 4 (2016) 145–151.
[31] X. Yang, X. Ma, J. Moering, H. Zhou, W. Wang, Y. Gong, J. Tao, Y. Zhu, X. Zhu, Influence of gradient structure volume fraction on the mechanical properties of pure copper, Mater. Sci. Eng. A 645 (2015) 280–285.
[32] X. Wu, P. Jiang, L. Chen, F. Yuan, Y.T. Zhu, Extraordinary strain hardening by gradient structure, Proc. Natl. Acad. Sci. 111 (2014) 7197–7201.
[33] J. Moering, X. Ma, J. Malkin, M. Yang, Y. Zhu, S. Mathaudhu, Synergetic strengthening far beyond rule of mixtures in gradient structured aluminum rod, Scr. Mater. 122 (2016) 106–109.
[34] X.L. Wu, M.X. Yang, F.P. Yuan, L. Chen, Y.T. Zhu, Combining gradient structure and TRIP effect to produce austenite stainless steel with high strength and ductility, Acta Mater. 112 (2016) 337–346.
[35] Q. He, Y.F. Wang, M.S. Wang, F.J. Guo, Y. Wen, C.X. Huang, Improving strength-ductility combination in 301 stainless steel by combining gradient structure and TRIP effect, Mater. Sci. Eng. A 780 (2020) 139146.
[36] Z. Cheng, H. Zhou, Q. Lu, H. Gao, L. Lu, Extra strengthening and work hardening in gradient nanotwinned metals, Science 362 (2018) eaau1925.
[37] Q. Pan, M. Yang, R. Feng, A.C. Chuang, K. An, P.K. Liaw, X. Wu, N. Tao, L. Lu, Atomic faulting induced exceptional cryogenic strain hardening in gradient cell–structured alloy, Science 382 (2023) 185–190.
[38] Y. Shi, A. Zhang, S. Liang, X. Zhang, S. Ren, H. Liu, D. Xu, X. Yang, Z. Xing, L. Wang, Activation of multiple deformation mechanisms and HDI hardening devoting to significant work-hardening of gradient-dislocation structured TRIP steel, Mater. Sci. Eng. A 893 (2024) 146131.
[39] Y. Wei, Y. Li, L. Zhu, Y. Liu, X. Lei, G. Wang, Y. Wu, Z. Mi, J. Liu, H. Wang, H. Gao, Evading the strength–ductility trade-off dilemma in steel through gradient hierarchical nanotwins, Nat. Commun. 5 (2014).
[40] C.W. Shao, P. Zhang, Y.K. Zhu, Z.J. Zhang, Y.Z. Tian, Z.F. Zhang, Simultaneous improvement of strength and plasticity: additional work-hardening from gradient microstructure, Acta Mater. 145 (2018) 413–428.
[41] C.X. Huang, W.P. Hu, Q.Y. Wang, C. Wang, G. Yang, Y.T. Zhu, An ideal ultrafine-grained structure for high strength and high ductility, Mater. Res. Lett. 3 (2014) 88–94.
[42] M.-M. Wang, C.C. Tasan, D. Ponge, A.-Ch Dippel, D. Raabe, Nanolaminate transformation-induced plasticity–twinning-induced plasticity steel with dynamic strain partitioning and enhanced damage resistance, Acta Mater. 85 (2015) 216–228.
[43] W. Lu, C.H. Liebscher, G. Dehm, D. Raabe, Z. Li, Bidirectional transformation enables hierarchical nanolaminate dual-phase high-entropy alloys, Adv. Mater. 30 (2018) 1804727.
[44] K. Ming, B. Li, L. Bai, P. Jiang, X. Wu, S. Zheng, J. Wang, Dynamically reversible shear transformations in a CrMnFeCoNi high-entropy alloy at cryogenic temperature, Acta Mater. 232 (2022) 117937.
[45] J. Su, X. Wu, D. Raabe, Z. Li, Deformation-driven bidirectional transformation promotes bulk nanostructure formation in a metastable interstitial high entropy alloy, Acta Mater. 167 (2019) 23–39.

[46] S. Harjo, N. Tsuchida, J. Abe, W. Gong, Martensite phase stress and the strengthening mechanism in TRIP steel by neutron diffraction, Sci. Rep. 7 (2017) 15149.
[47] J. Yan, W. Dong, P. Shi, T. Li, W. Liu, Y.-D. Wang, X.-L. Wang, Y. Zhu, Y. Ren, Synchrotron X-Ray study of heterostructured materials: a review, JOM 75 (2023) 1423–1434.
[48] W. Mao, S. Gao, W. Gong, T. Kawasaki, T. Ito, S. Harjo, N. Tsuji, Martensitic transformation-governed lüders deformation enables large ductility and late-stage strain hardening in ultrafine-grained austenitic stainless steel at low temperatures, Acta Mater. 278 (2024) 120233.
[49] B.E. Warren, X-ray Diffraction, 1990.
[50] W. Woo, J.S. Jeong, D.K. Kim, C.M. Lee, S.H. Choi, J.Y. Suh, S.Y. Lee, S. Harjo, T. Kawasaki, Stacking fault energy analyses of additively manufactured stainless steel 316L and CrCoNi medium entropy alloy using in situ neutron diffraction, Sci. Rep. 10 (2020) 2–4.
[51] X. Wu, M. Yang, R. Li, P. Jiang, F. Yuan, Y. Wang, Y. Zhu, Y. Wei, Plastic accommodation during tensile deformation of gradient structure, Sci. China Mater. 64 (2021) 1534.
[52] G. Frommeyer, U. Brux, P. Neumann, Supra-ductile and high-strength manganese-TRIP/TWIP steels for high energy absorption purposes, ISIJ Int. 43 (2003) 438.
[53] P. Wu, Y. Zhang, L. Han, K. Gan, D. Yan, W. Wu, L. He, Z. Fu, Z. Li, Unexpected sluggish martensitic transformation in a strong and super-ductile high-entropy alloy of ultralow stacking fault energy, Acta Mater. 261 (2023) 119389.
[54] G.B. Olson, M. Cohen, A general mechanism of martensitic nucleation: part II. FCC → BCC and other martensitic transformations. Metal, OR Trans. 7 (1976) 1905–1914.
[55] K.H. Kwon, B.-C. Suh, S.-I. Baik, Y.-W. Kim, J.-K. Choi, N.J. Kim, Deformation behavior of duplex austenite and ε-martensite high-Mn steel, Sci. Technol. Adv. Mater. 14 (2013) 014204.
[56] X.S. Yang, S. Sun, X.L. Wu, E. Ma, T.Y. Zhang, Dissecting the mechanism of martensitic transformation via atomic-scale observations, Sci. Rep. 4 (2014) 1–7.
[57] J. Hu, X. Li, Q. Meng, L. Wang, Y. Li, W. Xu, Tailoring retained austenite and mechanical property improvement in al–si–v containing medium Mn steel via direct intercritical rolling, Mater. Sci. Eng. A 855 (2022) 143904.
[58] Y. Shi, T. Wang, S. Liang, X. Zhang, D. Xu, H. Liu, A. Zhang, Z. Xing, L. Wang, An outstanding combination of high strength and ductility/toughness by combining gradient dislocation structure and DIM transformation, Mater. Today Commun. 35 (2023) 105666.
[59] Y. Shi, W. Shang, X. Zhang, S. Liang, S. Li, W. Chen, H. Liu, D. Xu, X. Liu, G. Lv, S. Wang, T. Guo, Z. Lv, Z. Xing, Superior mechanical properties and strengthening–toughening mechanisms of gradient-structured materials, Mater. Sci. Eng. A 861 (2022) 144365.
[60] D. Fahr, Stress- and strain-induced formation of martensite and its effects on strength and ductility of metastable austenitic stainless steels, Metall. Trans. A 2 (1971) 1883–1892.
[61] D.P. Yang, T. Wang, Z.T. Miao, P.J. Du, G.D. Wang, H.L. Yi, Effect of grain size on the intrinsic mechanical stability of austenite in transformation-induced plasticity steels: the competition between martensite transformation and dislocation slip, J Mater. Sci. Techl. 162 (2023) 38–43.
[62] T.H. Fang, N.R. Tao, Martensitic transformation dominated tensile plastic deformation of nanograins in a gradient nanostructured 316L stainless steel, Acta Mater. 248 (2023) 118780.
[63] Q. Pan, S. Guo, F. Cui, L. Jing, L. Lu, Superior strength and ductility of 304 austenitic stainless steel with gradient dislocations, Nanomaterials 11 (2021) 2613.
[64] G. Niu, H.S. Zurob, R.D.K. Misra, H. Wu, Y. Zou, Strength-ductility combination in a 1.4 GPa austenitic steel with a heterogeneous lamellar microstructure, J. Mater. Sci. Technol. 106 (2022) 133–138.
[65] L. Bracke, L. Kestens, J. Penning, Transformation mechanism of α'-martensite in an austenitic Fe–Mn–C–N alloy, Scr. Mater. 57 (2007) 385–388.
[66] W. Su, M. Wang, F. Guo, H. Ran, Q. Cheng, Q. Wang, Y. Zhu, X. Ma, C. Huang, Heterostructure enables anomalous improvement of cryogenic mechanical properties in titanium, Acta Mater. 273 (2024) 119982.
[67] P.L. Ferraglio, K. Mukherjee, The dynamics of nucleation and growth of a thermoelastic martensite in a splat quenched Au-47.5 at.% Cd alloy, Acta Met. 22 (1974) 835–845.
[68] J. Hu, X. Li, Z. Zhang, L. Wang, Y. Li, W. Xu, Overcoming the strength-ductility trade-off in metastable dual-phase heterogeneous structures using variable temperature rolling and annealing, Mater. Res. Lett. 11 (2023) 648–654.
[69] Y. Wang, M. Chen, F. Zhou, E. Ma, High tensile ductility in a nanostructured metal, Nature 419 (2002) 912–915.